



ANNUAL REVIEWS **Further**

Click here for quick links to Annual Reviews content online, including:

- Other articles in this volume
- Top cited articles
- Top downloaded articles
- Our comprehensive search

# Measurement of the $W$ Boson Mass at the Tevatron

Ashutosh V. Kotwal<sup>1</sup> and Jan Stark<sup>2</sup>

<sup>1</sup>Physics Department, Duke University, Durham, North Carolina 27708; email: kotwal@phy.duke.edu

<sup>2</sup>Laboratoire de Physique Subatomique et de Cosmologie, Université Joseph Fourier Grenoble 1, CNRS/IN2P3, Institut National Polytechnique de Grenoble, Grenoble, France; email: stark@in2p3.fr

Annu. Rev. Nucl. Part. Sci. 2008. 58:147–75

First published online as a Review in Advance on June 6, 2008

The *Annual Review of Nuclear and Particle Science* is online at [nucl.annualreviews.org](http://nucl.annualreviews.org)

This article's doi:  
10.1146/annurev.nucl.58.110707.171227

Copyright © 2008 by Annual Reviews.  
All rights reserved

0163-8998/08/1123-0147\$20.00

## Key Words

precision, electroweak, Higgs, new physics, supersymmetry

## Abstract

Over the past four decades, the standard model of electroweak interactions has achieved tremendous success in describing the experimental data. One of the key observables is the mass  $M_W$  of the  $W$  boson. The experimental measurements, including  $M_W$ , have reached a level of precision that tests the theory at the quantum loop level, providing indirect constraints on the hypothetical Higgs boson and other new physics. Improved measurements of  $M_W$  are driven by new data from Run II of the Fermilab Tevatron ( $p\bar{p}$  collider at  $\sqrt{s} = 1.96$  TeV). We discuss the techniques used for measuring  $M_W$  at hadron colliders, summarize the measurements from Run I of the Tevatron, and review the state of the art of the Run II analyses, which are based on significantly larger data sets collected with upgraded detectors. We discuss the constraints on the Higgs boson, and conclude with a discussion of the ultimate precision in  $M_W$  that can be expected from Run II.

## Contents

1. INTRODUCTION .....	148
1.1. Historical Overview .....	149
1.2. Electroweak Theory .....	149
2. FINAL LEP MEASUREMENTS .....	151
3. MEASUREMENT TECHNIQUES AT HADRON COLLIDERS .....	152
4. TEVATRON RUN I $W$ MASS MEASUREMENTS .....	154
4.1. CDF and DØ Run I Detectors .....	154
4.2. CDF and DØ Analysis Methodology .....	155
4.3. Results and Systematics .....	156
4.4. Scaling of Collider Data-Driven Systematics .....	158
4.5. External Inputs to Systematics .....	158
5. TEVATRON RUN II $W$ MASS ANALYSES .....	159
5.1. CDF and DØ Run II Detector Upgrades .....	159
5.2. Impact of Upgrades on Analysis Methodology .....	160
5.3. Details of the CDF Run II Analysis .....	164
5.4. Calibrations in the CDF Analysis .....	165
5.5. Calibrations in the DØ Analysis .....	167
5.6. Backgrounds .....	167
5.7. Production and Decay Model .....	168
6. WHAT HAVE WE LEARNED ABOUT THE HIGGS AND OTHER NEW PHYSICS? .....	169
7. ULTIMATE $M_W$ PRECISION FROM THE TEVATRON RUN II .....	171
8. SUMMARY .....	172

## 1. INTRODUCTION

In its four decades of existence, the standard model (SM) of the electroweak interactions has been an impressive success. The massive  $W$  and  $Z$  bosons that it predicted have since been discovered. In the SM, the mass of the  $W$  boson,  $M_W$ , is related at tree level to the mass of the  $Z$  boson,  $M_Z$ , and the electromagnetic (EM) and weak coupling constants. Given the precise measurements of the latter quantities, plus experimental determinations of the weak mixing angle from scattering data available at the time, the masses of both the  $W$  boson and the  $Z$  boson can be predicted to within a few gigaelectronvolts (GeV).<sup>1</sup> The agreement of these predictions with the early measurements is one of SM's successes. The precision of the direct measurements of  $M_W$  and  $M_Z$  has increased dramatically over the past 25 years, and the predictions are now being tested at the quantum loop level. In the SM, the quantum loop corrections to  $M_W$  are dominated by the top quark and Higgs boson loops, aside from the running of the electromagnetic coupling. Extensions to the SM (e.g., supersymmetry) predict additional loops that can result in sizeable corrections. Even more precise measurements of  $M_W$  are needed to test the SM at the loop level and to fully exploit this window on physics beyond the SM.

<sup>1</sup>Throughout this review we use units of  $\hbar = c = 1$ .

A previous review of direct experimental determinations of  $M_W$  was published in 2000 (1). At that time the most precise measurements available were from Run I of the Tevatron and from the Large Electron-Positron Collider (LEP). The analyses of the Tevatron Run I data were then being finalized and LEP was about to finish collecting data. As of now the Tevatron is operating again, and the results from Run II will drive the precision on  $M_W$  for at least the next few years. These data are the focus of this review.

## 1.1. Historical Overview

The electroweak  $SU(2) \times U(1)$  gauge theory, which unifies the weak and EM forces, was proposed in 1967 (2). In this theory the weak force is mediated by the massive  $W$  and  $Z$  bosons. In 1983 this central prediction was confirmed by the discovery (3, 4) of the  $W$  boson (with a mass of  $81 \pm 5$  GeV) and the discovery of the  $Z$  boson just months later (5, 6) by the UA1 and UA2 experiments at the European Organization for Nuclear Research (CERN)  $S\bar{p}\bar{p}S$  collider ( $p\bar{p}$  at  $\sqrt{s} = 546$  GeV). More precise measurements of the  $W$  boson mass were performed by UA1 (7) and UA2 (8) with upgraded detectors and much larger data sets delivered by the upgraded  $S\bar{p}\bar{p}S$  operating at  $\sqrt{s} = 630$  GeV. UA2 performed the first measurement with a precision better than 1 GeV (8). Shortly thereafter the Collider Detector at Fermilab (CDF) and  $D\bar{O}$  experiments at the Fermilab Tevatron collider ( $p\bar{p}$  at  $\sqrt{s} = 1.8$  TeV) pushed the precision below 100 MeV (9–12) using data from Run I (1992–1995) of the Tevatron, achieving a combined precision of 59 MeV (13). At about the same time, the LEP at CERN became the first  $e^+e^-$  collider to operate above the  $e^+e^- \rightarrow W^+W^-$  threshold. The combined measurements of  $M_W$  from the Apparatus for LEP Physics at CERN (ALEPH), Detector with Lepton, Photon, and Hadron Identification (DELPHI), L3, and Omni-Purpose Apparatus for LEP (OPAL) experiments at the LEP have an uncertainty of 33 MeV (14). Since 2001 the upgraded CDF and  $D\bar{O}$  experiments have been taking data at Run II of the upgraded Tevatron at  $\sqrt{s} = 1.96$  TeV, and they are further improving our knowledge of  $M_W$ .

## 1.2. Electroweak Theory

In the “on-shell” scheme, the  $W$  boson mass can be written as

$$M_W^2 \left( 1 - \frac{M_W^2}{M_Z^2} \right) = \frac{\pi\alpha}{\sqrt{2}G_F} \left( \frac{1}{1 - \Delta r} \right),$$

where  $\alpha$  is the EM coupling at the renormalization energy scale  $Q = M_Z$  and  $G_F$  is the Fermi weak coupling extracted from the muon lifetime (see Reference 15; also see Reference 1 for a concise overview). The term  $\Delta r$  includes all radiative corrections, i.e.,  $\Delta r = 0$  corresponds to the tree level result. In the SM, the corrections can be separated into three main pieces:

$$\Delta r = \Delta\alpha + \Delta\rho[(M_{\text{top}}/M_Z)^2] + \Delta\chi[\ln(M_H/M_Z)].$$

The contribution  $\Delta\alpha$  represents the running of the EM coupling due to the light quarks. The contribution  $\Delta\rho$ , which depends on the top quark mass ( $M_{\text{top}}$ ) as  $M_{\text{top}}^2$ , arises from loops containing the top and bottom quarks (**Figure 1**). The contribution  $\Delta\chi$  and its logarithmic dependence on the Higgs boson mass  $M_H$  arise from the Higgs loops (shown in **Figure 2**). Additional contributions to  $\Delta r$  arise in extensions of the SM: For example, contributions from supersymmetric particles are dominated by squark loops (**Figure 3**). Generally, the lighter the squark masses and the larger the

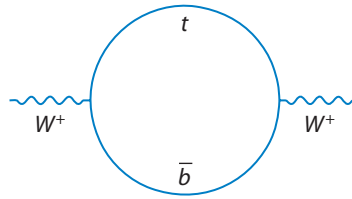


**Figure 1**

The one-loop contribution to the  $W$  boson mass from top and bottom quarks. Reproduced from Reference 20 with permission.

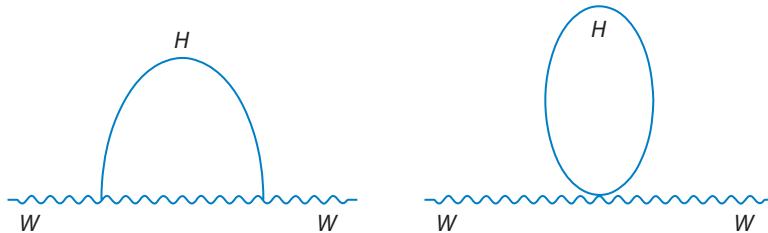


**Figure 2**

Higgs one-loop contributions to the  $W$  boson mass. Reproduced from Reference 20 with permission.

squark weak doublet mass splitting, the larger the contribution to  $M_W$ . Supersymmetric particles can induce a total radiative correction to  $M_W$  of several hundred megaelectronvolts (MeV) (16).

In the framework of the SM, precise measurements of  $M_{\text{top}}$  and  $M_W$  can be translated into a constraint on the mass of the as-yet-unobserved Higgs boson. The experimental uncertainties  $\Delta M_{\text{top}}$  and  $\Delta M_W$  contribute equally to the uncertainty  $\Delta M_H$  on the predicted Higgs mass if  $\Delta M_W \simeq 0.006 \cdot \Delta M_{\text{top}}$  (17). The uncertainties from experimental determinations of the other parameters (17) and from higher order corrections (17) will not be a limiting factor in the foreseeable future. The current combined Tevatron results on  $M_{\text{top}}$  have an uncertainty  $\Delta M_{\text{top}} = 1.8 \text{ GeV}$  (18), which is expected to be further reduced as more data from Run II are analyzed. For this  $\Delta M_{\text{top}}$ , the equivalent  $\Delta M_W$  for equal contribution to  $\Delta M_H$  would be  $\Delta M_W \simeq 11 \text{ MeV}$  (17), which is smaller than the current experimental error on  $M_W$  by more than a factor of two; the latter is therefore the limiting factor in precision tests and must be reduced.

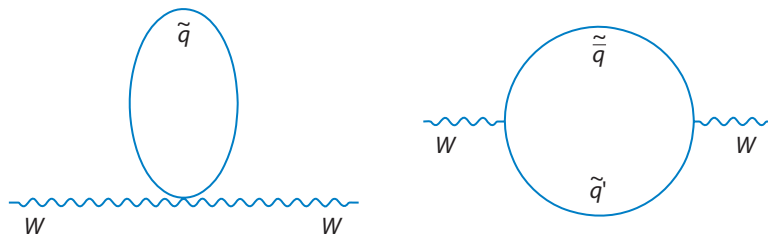


**Figure 3**

One-loop squark contributions to the  $W$  boson mass. Reproduced from Reference 20 with permission.

## 2. FINAL LEP MEASUREMENTS

Before we discuss the  $M_W$  measurements at the Tevatron in detail, we summarize the final results from LEP. From 1989 to 1995, the LEP at CERN provided  $e^+e^-$  collisions at center-of-mass energies at or near the  $Z$  boson mass. The four experiments—ALEPH, DELPHI, L3, and OPAL—have published their final results and combinations (21) based on the  $Z$  pole data set. These results are critical in the context of our review because they include a precise measurement of the  $Z$  boson mass (used to calibrate the absolute energy scale in many Tevatron measurements) and a wealth of other inputs to the SM fits discussed in Section 6.

From 1996 to 2000 LEP ran at center-of-mass energies above the  $W$  pair production threshold,  $\sqrt{s} > 2M_W$ . At these energies LEP produced significant samples of  $W$  bosons, predominantly in pairs:  $e^+e^- \rightarrow W^+W^-$ . There are two main methods of measuring  $M_W$  in these data sets, both of which have been discussed in another review (1). The first method exploits the fact that the  $W^+W^-$  production cross section is particularly sensitive to  $M_W$  in the threshold region. The final results, based on roughly  $10 \text{ pb}^{-1}$  of data at  $\sqrt{s} \simeq 161 \text{ GeV}$  per experiment (22–25), are (14)

$$M_W = 80,400 \pm 200(\text{stat}) \pm 70(\text{syst}) \pm 30(E_{\text{beam}}) \text{ MeV.}$$

At energies significantly above the  $W^+W^-$  threshold,  $M_W$  is measured through the direct reconstruction of the invariant mass of  $W$  boson candidates from measured jets and leptons. The principle and the earlier versions of these measurements, based on subsets of the LEP data, have been discussed before (1). Since then, all four collaborations have published their final measurements (26–29) based on the full data set of about  $700 \text{ pb}^{-1}$  per experiment. The combination (14)

$$M_W = 80,375 \pm 25(\text{stat}) \pm 22(\text{syst}) \text{ MeV,}$$

however, uses only a preliminary combined estimate for the effect of color reconnection (CR). This result is significantly more precise than that from the threshold analysis cited above. A breakdown of the uncertainties (14) is summarized in **Table 1**. Compared to the time of the last review (1), the statistical uncertainties have been substantially reduced. Furthermore, important reductions in the systematic uncertainties have been achieved so that they are comparable in magnitude to the statistical uncertainties. In particular, the estimates of the LEP beam energy and of the effects of fragmentation, Bose–Einstein correlations (BE), and CR have been significantly improved.

As the typical decay distance of the  $W$  boson,  $\Gamma_W^{-1} \simeq 0.1 \text{ fm}$ , is small compared to the typical fragmentation radius,  $\Lambda_{\text{QCD}}^{-1} \simeq 1 \text{ fm}$ , the hadronic decay products from the two different  $W$  bosons in  $e^+e^- \rightarrow W^+W^- \rightarrow q\bar{q}q\bar{q}$  cannot be modeled as independent. The BE and CR mechanisms are the dominant sources of correlation. The LEP collaborations have performed extensive studies (see Reference 14 and references therein) of BE and CR to quantify the effect on the  $M_W$  measurements. Furthermore the final measurements in the  $q\bar{q}q\bar{q}$  channel use selection criteria that reduce the effect of BE and CR at the expense of some statistical power. The preliminary combination (14) of the LEP results based on the two methods yields

$$\begin{aligned} M_W &= 80,376 \pm 25(\text{stat}) \pm 22(\text{syst}) \text{ MeV,} \\ &= 80,376 \pm 33 \text{ MeV.} \end{aligned}$$

At the time of this review [i.e., with one Run II result based on  $200 \text{ pb}^{-1}$  of CDF data (19, 20) available], these data are still more precise than the combined Tevatron results.

**Table 1** Summary of uncertainties in the combined LEP measurement of  $M_W$  based on direct mass reconstruction in the  $W^+W^- \rightarrow q\bar{q}l\bar{\nu}_l$  and  $W^+W^- \rightarrow q\bar{q}q\bar{q}$  channels

Source	Systematic error on $M_W$ (MeV)		
	$q\bar{q}l\bar{\nu}_l$	$q\bar{q}q\bar{q}$	Combined
ISR/FSR	8	5	7
Hadronization	13	19	14
Detector systematics	10	8	10
LEP beam energy	9	9	9
Color reconnection	–	35	8
Bose–Einstein correlations	–	7	2
Other	3	11	4
Total systematic	21	44	22
Statistical	30	40	25
Total	36	59	33

Abbreviations: FSR, final-state radiation; ISR, initial-state radiation.

### 3. MEASUREMENT TECHNIQUES AT HADRON COLLIDERS

Two hadron colliders have provided collisions at sufficient center-of-mass energies to produce on-shell  $W$  bosons: the CERN  $S\bar{p}\bar{p}S$  and the Fermilab Tevatron. (See References 1 and 10 for Feynman diagrams for  $W$  and  $Z$  boson production at hadron colliders.)  $Z$  bosons provide a crucial control sample that is used in the tuning of many key aspects of the detector model for the measurement of the  $W$  boson mass. At hadron colliders measurements of the  $W$  boson mass are performed in the leptonic  $W \rightarrow e\nu$  and  $W \rightarrow \mu\nu$  channels.<sup>2</sup> Decays to quark pairs are not useful for this purpose, given the large direct  $q\bar{q}'$  background from quantum chromodynamics (QCD) processes. Electrons and muons are relatively easy to identify and trigger on, and their kinematic properties can be measured precisely. Hadronic decays of the  $\tau$  lepton are difficult to identify. The leptonic decays of the  $\tau$  lepton are considered backgrounds to the electron and muon channels. The branching ratio  $\mathcal{B}$  for each lepton decay  $W \rightarrow \ell\nu$  ( $Z \rightarrow \ell\ell$ ) is approximately 11% (3.3%). The  $W$  boson production cross sections  $\sigma$  at  $p\bar{p}$  colliders are large:  $\sigma \cdot \mathcal{B} \simeq 680$  pb at  $\sqrt{s} = 630$  GeV (30), 2.3 nb at  $\sqrt{s} = 1.8$  TeV (31), and 2.8 nb at  $\sqrt{s} = 1.96$  TeV (32). The corresponding values for  $Z$  bosons are about ten times smaller, e.g.,  $\sigma \cdot \mathcal{B} \simeq 0.25$  nb at  $\sqrt{s} = 1.96$  TeV (32).

The Large Hadron Collider (LHC) at CERN ( $p\bar{p}$  at  $\sqrt{s} = 14$  TeV) is expected to deliver its first collisions later in 2008. At the LHC,  $\sigma \cdot \mathcal{B}(W \rightarrow \ell\nu) \simeq 20$  nb (33). An integrated luminosity of  $10 \text{ fb}^{-1}$  could be accumulated in one year of low-luminosity running at the LHC. Such an accumulation would lead to  $W \rightarrow \ell\nu$  and  $Z \rightarrow \ell\ell$  samples of unprecedented size, and the LHC experiments are expected (33–35) to contribute precision measurements of  $M_W$  once the detectors are well understood.

In this review, we use a right-handed coordinate system that has its origin at the nominal average  $p\bar{p}$  collision point. The  $z$  axis points in the direction of the proton beam, the  $y$  axis points upwards, and the  $x$  axis points horizontally. With respect to the  $z$  axis,  $\theta$  is the polar angle,  $\phi$  denotes the azimuthal angle, and  $r$  denotes the distance from the  $z$  axis. Because the longitudinal momenta  $p_Z$  of the interacting partons are not known on a per-event basis, one generally works with momenta transverse to the beam line. Lepton momenta are denoted  $\vec{p}$  and the corresponding transverse momenta are denoted  $\vec{p}_T$ , with magnitude  $p_T = |\vec{p}_T|$ . Energy is denoted  $E$  and the lepton masses

<sup>2</sup>Throughout this review, references to a lepton or to a  $W$  decay reaction also imply their charge conjugate.

are neglected. The rapidity  $y = \frac{1}{2} \ln[(E + p_z)/(E - p_z)]$  is additive under Lorentz boosts along the  $z$  axis. For massless particles this quantity is equal to the pseudorapidity  $\eta = \ln[\cot(\theta/2)]$ .

The momentum  $\vec{p}(\ell)$  of the charged lepton from the  $W$  boson decay is measured with good precision, whereas the neutrino escapes detection. Its presence is inferred from an apparent imbalance in the net observed transverse momentum. The hadronization of the  $p$  and  $\bar{p}$  fragments and of any quarks or gluons from the hard scatter typically leads to a large number of hadrons in the final state. Some of them escape through the beam pipe and are not detected. Although these particles may carry substantial  $p_z$ , they carry little  $p_T$ . No attempt is made to detect these particles individually in the  $W$  boson mass analysis; instead the calorimeter is used to obtain an approximate measurement of their vectorially summed transverse momentum. Specifically, one defines

$$\vec{u}_T = \sum_i E_i \sin \theta_i \hat{i},$$

where the sum runs over all calorimeter cells that are not included in the lepton cluster,  $E_i$  is the energy in cell  $i$ , and the unit vector  $\hat{i}$  provides the cell's transverse direction from the beam axis. The observable  $\vec{u}_T$ , often referred to as hadronic recoil, is used to infer the transverse momentum of the  $W$  boson ( $\vec{p}_T(W) = -\vec{u}_T$ ) and the neutrino ( $\vec{p}_T(\nu) = -\vec{u}_T - \vec{p}_T(\ell)$ ). Researchers use this technique because the most reliable calculations and parameterizations of the hadronic activity are those for the fully inclusive measurement of  $p_T(W)$ , rather than a measurement based on (for example) reconstructed jets. To summarize, the basic observables are the measured  $\vec{p}(\ell)$  and  $\vec{u}_T$  and the inferred quantities are  $\vec{p}_T(\nu)$  and  $\vec{p}_T(W)$ .

For studies of the  $Z$  boson in  $Z \rightarrow \ell\ell$ , the invariant mass of the lepton pair is a key observable. The invariant mass of  $W$  bosons in  $W \rightarrow \ell\nu$  cannot be reconstructed because  $p_z(\nu)$  is not measured. Instead, the most precise measurements of  $M_W$  are based on the transverse mass  $m_T$ :

$$m_T = \sqrt{2p_T(\ell)p_T(\nu)\{1 - \cos[\phi(\ell) - \phi(\nu)]\}}.$$

This variable has the advantage that its spectrum is relatively insensitive to the production dynamics of the  $W$  boson. Relative contributions to  $m_T$  due to the motion of the  $W$  boson are of  $\mathcal{O}((p_T(W)/M_W)^2)$ . But because  $m_T$  uses the inferred neutrino momentum, it is sensitive to the details of the recoil measurement (see Reference 10, Figure 3). Alternatively  $M_W$  can be extracted from the lepton  $p_T$  spectrum (see Reference 10, Figure 4), which is indirectly sensitive to the recoil measurement (via any  $u_T$  requirement in the event selection). Its shape, however, is sensitive to the motion of the  $W$  boson and receives corrections of  $\mathcal{O}(p_T(W)/M_W)$ . Examples from the CDF Run II analysis (which we discuss in detail below) are shown in **Figure 4**. The spectrum of the inferred neutrino  $p_T$  is sensitive to both effects. The  $p_T(\ell)$ ,  $p_T(\nu)$ , and  $m_T$  distributions exhibit the Jacobian edge (e.g., at about half the  $W$  boson mass in the  $p_T$  spectra) that characterizes all two-body decays (36). This part of the measured distributions carries most of the sensitivity to  $M_W$ . Because the Jacobian edge is smeared out by the boson  $p_T$ , events with large  $p_T(W)$  are not useful for the mass measurement. Event selection is typically based on lepton identification and simple kinematic criteria, such as  $p_T(\ell) > 25$  GeV,  $p_T(\nu) > 25$  GeV, and  $p_T(W) < 15$  GeV, which preserve the Jacobian edge.

The radiation of quarks and gluons off the initial-state partons (known as initial-state radiation, or ISR) imparts a transverse boost to the  $W \rightarrow \ell\nu$  system. Fortunately the typical ISR  $p_T$  is small,  $\mathcal{O}(10$  GeV), and events with large ISR activity (observed as large  $u_T$ ) are rejected. Furthermore the transverse direction of  $\vec{p}_T(W)$  is largely uncorrelated with the leptons' transverse directions after the  $W$  boson decay, so that the average component of  $\vec{p}_T(W)$  in the lepton direction is  $\mathcal{O}(0.2$  GeV). As this average is small compared to the lepton  $p_T(\ell) \sim 40$  GeV, the sensitivity of the  $W$  boson mass measurement to the hadronic response calibration is suppressed. Nevertheless a

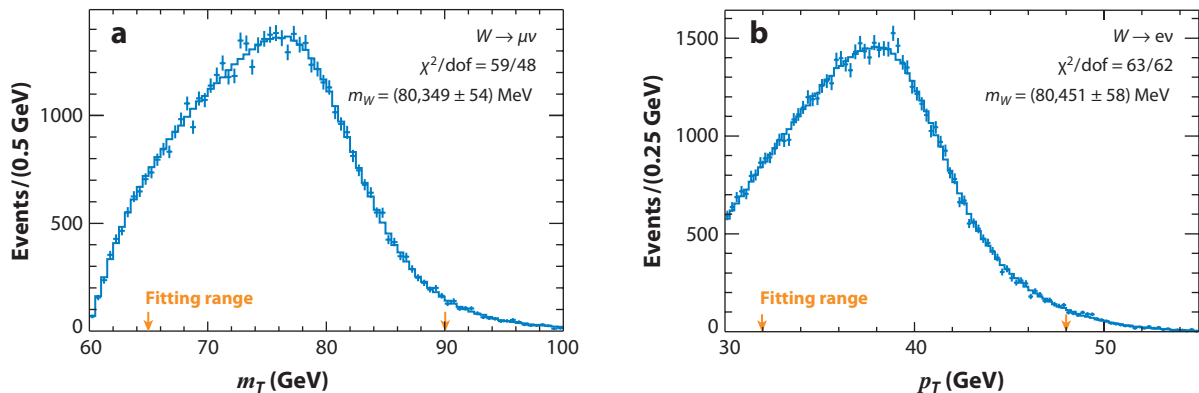


**Figure 4**

The distribution of the data (*points*) and the best-fit simulation template including backgrounds (*histogram*) for  $m_T(\mu\nu)$  (a) and  $p_T(e)$  (b) from the Collider Detector at Fermilab Run II analysis (19, 20). The orange arrows indicate the fitting range. The best-fit values of  $M_W$  and statistical uncertainty are shown, along with the  $\chi^2$  between the data and the template per degree of freedom in the fitting range.

careful measurement of the hadronic response and resolution at the  $\mathcal{O}(1\%)$  level is needed so that it does not dominate the mass measurement uncertainty. To first order, the fractional uncertainty in the lepton energy scale translates directly into a fractional uncertainty on  $M_W$ , i.e., lepton energy scale calibrations at the few- $10^{-4}$  level are needed.

The convolution of the boson production and decay with the detector response results in observed  $p_T(\ell)$ ,  $p_T(\nu)$ , and  $m_T$  spectra that cannot be calculated analytically. Instead one uses detailed Monte Carlo simulations (see, e.g., References 9–12, 19, 20) that incorporate the generator-level production and decay physics and a parameterized detector response. These simulations are used to generate high-statistics templates of the observed kinematic spectra, one template for each assumed value of the  $W$  boson pole mass. A maximum likelihood fitting technique is then used to select the template that best matches the data. Because templates must be generated frequently, the simulations are customized for lepton and recoil simulation at high speed. Detailed calculations using first principles are used for some aspects of lepton response, but most of the detector simulation (e.g., selection efficiencies and recoil response and resolution) is based on parameterized models. These models are tuned primarily using dilepton resonances (especially  $Z \rightarrow \ell\ell$ ) in collider data. The analysis technique affords a large number of comparisons and cross checks between simulation and data so as to confirm that the simulation quantitatively reproduces all the features of the data.

## 4. TEVATRON RUN I $W$ MASS MEASUREMENTS

CDF performed a measurement of the  $W$  mass from the 1988–1989 data (Run 0), and both CDF and DØ performed measurements from the 1992–1995 data (Run I). Although some of these measurements have been discussed before (1), it is useful to compare and contrast the Run I and Run II analyses.

### 4.1. CDF and DØ Run I Detectors

The CDF (9, 37) and DØ (10–12, 38) detectors used in Run I are similar in some respects and fundamentally different in others. Both detectors exploited a cylindrical geometry with the beam running along its axis, and both used tracking devices surrounded by EM and hadronic calorimeters

and muon detectors. In addition to the barrel detectors, CDF and DØ exploited forward end-cap detectors to maximize the acceptance in rapidity.

The primary difference between the CDF and DØ detectors in Run I was that CDF used a magnetic spectrometer for tracking charged particles and measuring their momenta. A 1.4-T axial magnetic field was generated by a superconducting solenoid placed between the tracking detectors and the EM calorimeter. The radius of the solenoid was 1.5 m, which provided a large tracking volume occupied by a drift chamber for reconstructing the helical trajectories of charged particles. The drift chamber tracking and momentum measurement played a key role in the CDF Run I measurement of the  $W$  boson mass in the muon channel. The magnetic tracker also played a key role in calibrating the nonlinearity of the lead-scintillator EM calorimeter using the in situ sample of electrons from  $W$  boson decays. Wire and strip chambers placed at the location of the EM shower maximum provided finer transverse segmentation for particle identification using shower profile measurements. The combination of the latter with the ratio of EM energy to track momentum and with the fraction of hadronic energy provided good electron-jet discrimination. Thus CDF used both the electron and the muon channels for the  $W$  boson mass measurement.

The most important component of the DØ Run I detector from the perspective of the  $W$  boson mass measurement was the hermetic uranium/liquid argon (U/LAr) sampling calorimeter covering  $|\eta| < 4$ . This calorimeter enclosed a nonmagnetic tracker consisting of drift and vertex chambers that were used to measure the directions of charged particles. The choice of the U/LAr technology for calorimetry allowed for a compact device with a good sampling fraction and wide angular coverage and depth, as well as fine transverse and longitudinal segmentation. The unit-gain charge readout of the active material provided a high level of stability and uniformity and contributed strongly to the calorimeter's linear response for high-energy electrons. The fine segmentation of the readout enabled the use of sophisticated shower-shape discriminants to reject fake electron candidates from QCD jets, and the hadronic sections provided hermetic coverage without projective cracks. Together with the wide angular coverage and the relatively good response and resolution of the U/LAr technology, these attributes led to good resolution on missing  $E_T$ . These features of the DØ calorimeter, in particular the high-energy linearity of the EM calorimeter, were primarily responsible for the  $W$  boson mass measurements by DØ in Run I, which used  $W$  boson decays to electrons in both the central-rapidity and forward-rapidity regions.

## 4.2. CDF and DØ Analysis Methodology

Various techniques have been used to calculate the generator-level lepton momentum vectors and  $\vec{p}_T(W)$ . These techniques range from the use of customized matrix-element calculations augmented with ad hoc parameterizations of the  $p_T(W)$  spectrum to the use of specialized programs such as The Monte Carlo for Resummed Boson Production and Decay (ResBos) (39). ResBos and similar programs (40) calculate the quintuple differential cross section  $d\sigma/dm dq_T dy d\Omega$  for  $W$  and  $Z$  boson production, where  $m$ ,  $q_T$ , and  $y$  are the boson invariant mass, transverse momentum, and rapidity, respectively, and where  $\Omega$  is the solid angle of the decay leptons in the boson rest frame. The  $q_T$  spectrum includes contributions from fixed-order matrix elements at high  $q_T$  matched to a resummation calculation at intermediate  $q_T$  and a nonperturbative form factor at low  $q_T$ . As in the case of the ad hoc parameterization of the  $p_T(W)$  spectrum, the parameters of the nonperturbative form factor are tuned to fit the data. In the case of the ad hoc parameterization (9), the collider  $Z \rightarrow \ell\ell$  data are used, along with theoretical information on the ratio of the  $W$  and  $Z$  boson  $p_T$  spectra. In the case of the ResBos parameterization, the collider  $Z \rightarrow \ell\ell$  data

are also used (10, 19, 20), along with constraints from global fits to data on Drell–Yan and direct photon production.

In the Run I analysis CDF extensively studied the lepton momentum scale by (a) using the  $J/\psi \rightarrow \mu\mu$  and  $\Upsilon \rightarrow \mu\mu$  mass measurements for calibration and then (b) transferring the tracker momentum scale to the EM calorimeter using a fit to the distribution of the ratio of calorimeter energy to track momentum ( $E/p$ ) for electrons from  $W \rightarrow e\nu$  decays. Due to a significant discrepancy between the  $Z \rightarrow ee$  mass measurement and the known value from the LEP, the lepton calibrations based on the  $J/\psi$  and  $\Upsilon \rightarrow \mu\mu$  data and the  $E/p$  fit ultimately were not used for the  $W$  boson mass measurement (9); instead the calibrations based on the  $Z \rightarrow \mu\mu$  and  $Z \rightarrow ee$  mass measurements were used for the respective channels. DØ also used the EM calorimeter calibration based on the  $Z \rightarrow ee$  mass measurement, along with lower energy constraints on the response nonlinearity from  $\pi^0 \rightarrow \gamma\gamma$  and  $J/\psi \rightarrow ee$  data. Both experiments constrained the lepton energy resolution models using the observed width of the  $Z$  boson mass peaks. The imposition of  $p_T$  balance in  $Z$  boson events was used to tune the parameterized models of the hadronic response and resolution. The latter also included a contribution from the spectator parton interactions accompanying the hard scatter, as well as from additional  $p\bar{p}$  collisions.

### 4.3. Results and Systematics

CDF and DØ each collected  $\approx 100 \text{ pb}^{-1}$  of data at  $\sqrt{s} = 1.8 \text{ TeV}$  during Run I. Using both electron and muon decays in the central detector, CDF measured

$$M_W = 80,433 \pm 79 \text{ MeV}.$$

DØ used electron decays in the central- and forward-rapidity regions to measure

$$M_W = 80,483 \pm 84 \text{ MeV}.$$

The CDF result was based on the  $m_T$  fit, whereas the DØ result was based on a combination of the  $m_T$ ,  $p_T(e)$ , and  $p_T(\nu)$  fits. This combination was performed with the best linear unbiased estimator (BLUE) method (41), taking into account all correlations.

**Tables 2 and 3** summarize the uncertainties that contributed to the CDF and DØ measurements from the 1994–1995 data (9–12). In addition to the statistical uncertainty from the  $W$  boson distributions, the lepton and hadronic calibrations and resolution models are uncorrelated between the two detectors for the purpose of combining their measurements (13). The lepton identification requirements have an efficiency that is mildly correlated with the hadronic activity in the vicinity of the lepton. This hadronic activity therefore induces a correlation between the lepton identification efficiency and the lepton  $p_T$  and sculpts the kinematic distributions from which the  $W$  boson mass is extracted. The measurement of this selection bias is uncorrelated between experiments. Similarly the background normalizations and shapes are measured independently and are incorporated into the simulation templates. The constraints on the  $p_T(W)$  spectrum were derived largely from each experiment’s own data, hence the corresponding uncertainty has also been treated as an uncorrelated uncertainty in the combination of CDF and DØ measurements (13).

The sources of uncertainties that have been taken as correlated (13) between the CDF and DØ Run I analyses are shown in **Table 3**. At hadron colliders the parton distribution functions (PDFs), i.e., the momentum densities of the partons annihilating to produce the  $W$  boson, influence the mass fit in two ways. First, the PDFs convolute to generate the mass-dependent parton luminosity that multiplies the Breit–Wigner mass distribution. Second, the PDFs govern the distribution of

**Table 2** Uncorrelated uncertainties (MeV) in the  $W$  boson mass measurements from CDF and DØ data collected from 1994 to 1995

Source	CDF $\mu$	CDF $e$	DØ $e$
$W$ boson statistics	100	65	60
Lepton momentum scale	85	75	56
Lepton momentum resolution	20	25	19
Theoretical $p_T(W)$ spectrum	20	15	15
Detector recoil response and resolution model	35	37	35
Selection bias	18	–	12
Backgrounds	25	5	9

Electron ( $e$ ) and muon ( $\mu$ ) decay channels are listed separately. Table reproduced from Reference 13.

the boson’s longitudinal momentum. The limited lepton acceptance in rapidity causes the transverse kinematics to be correlated with the longitudinal momentum distribution. The correlation weakens as the rapidity coverage becomes more inclusive; in the limit of complete rapidity coverage the transverse kinematics and hence the  $W$  boson mass fits become independent of the boson’s longitudinal momentum. As **Table 3** shows, the PDF uncertainty in the DØ measurement was smaller than that of CDF because of DØ’s use of electrons up to  $|y(\ell)| \approx 2.5$  (in comparison with CDF’s use of leptons up to  $|y(\ell)| \approx 1$ ). The PDFs are determined from global fits to data from many experiments.

Another source of correlated uncertainty is quantum electrodynamics (QED) radiative corrections. Photon radiation emanates from the initial-state quarks, the  $W$  boson propagator, and the final-state charged lepton. By far the dominant effect on the  $W$  boson mass fit comes from the photon radiation off the charged lepton (known as final-state radiation, or FSR), which reduces  $p_T(\ell)$  and shifts the fitted mass down. Due to their smaller mass, electrons radiate substantially more than muons; however this enhancement occurs for small angular separation between the lepton and the photon. The small-angle radiation is coalesced by the calorimeter cluster, whose typical angular radius in  $\eta - \phi$  space is  $\mathcal{O}(0.2)$ . The wide-angle radiation, which is similar for electrons and muons, causes a shift in the measured  $W$  boson mass by  $\mathcal{O}(100 \text{ MeV})$ . The simulation programs incorporated the calculation of radiative corrections (42, 43), which was cross-checked against other programs including PHOTOS (44) and WGRAD (45).

Because the  $W$  boson mass information is extracted from  $m_T$  or  $p_T$  distributions with one-sided Jacobian edges, the mass fit is influenced by the boson’s decay width. In Run I analyses CDF and DØ used different conventions: CDF used the SM calculation of the width in the simulation with negligible uncertainty, whereas DØ used the world-average measured value and its uncertainty. For the purpose of combination (13), the correlated uncertainty was taken to be the uncertainty due to the measured world average.

**Table 3** Correlated sources of systematic uncertainties (MeV) in the  $W$  boson mass measurements from CDF and DØ Run I

Source	CDF	DØ
PDF and parton luminosity	15	8
QED radiative corrections	11	12
$\Gamma_W$	10	10

Table reproduced from Reference 13. Abbreviations: PDF, parton distribution function; QED, quantum electrodynamics.

#### 4.4. Scaling of Collider Data-Driven Systematics

In Run I the calibration of the lepton energy and the hadronic recoil was based on the boson data and was expected to scale with boson statistics. This was also true for the lepton and hadronic resolution models. However there are scenarios wherein these uncertainties scale faster or slower than boson statistics. If multiple collider data sets were to provide a self-consistent analysis model, inclusion of these data would improve the  $W$  boson mass uncertainty compared to, say, using  $Z$  boson events alone. On the other hand, reduced detector resolutions due to less-favorable running conditions can reduce the statistical power of each  $Z$  boson event. Even more importantly, at higher levels of precision the parameterizations of response and resolution may need to become more complicated in order to capture subtle effects, increasing the number of degrees of freedom to be constrained by collider data. These effects retard the scaling improvement of the  $W$  boson mass uncertainty. We discuss these two scenarios in Sections 5 and 7 below.

The selection bias is measured with  $Z$  boson events: An event can be selected with tight cuts on one lepton with the other unbiased lepton used to probe the identification efficiency. The uncertainty on the selection bias is likely to scale with statistics. Backgrounds are estimated using a combination of data-based techniques for misidentification backgrounds (such as those arising from QCD jets) and detailed simulations of SM processes that yield the  $\ell\nu$  final state (such as the  $W \rightarrow \tau\nu \rightarrow \ell\nu\bar{\nu}$  process). The misidentification backgrounds tend to be more difficult to pin down, and their uncertainties do not automatically scale with statistics. The typical method of determining these background uncertainties is to compare the estimates obtained using different data-based techniques. More data will allow these techniques to be improved. In addition higher signal statistics allow more stringent identification requirements, and misidentification backgrounds are correspondingly suppressed.

The theoretical boson  $p_T$  spectrum can be constrained quite precisely by the measurement of the  $Z$  boson  $p_T$  using the well-measured dileptons; the measurement of  $p_T(W)$  using the hadronic recoil is strongly influenced by the latter's calibration and resolution and does not provide a reliable measurement of the theoretical boson  $p_T$  spectrum, especially at low  $p_T$ . Hence the measurement of the  $p_T(Z)$  spectrum will continue to improve with statistics. Given the parameterizations in use, the translation of the  $p_T(Z)$  spectrum to the theoretical  $p_T(W)$  spectrum has not incurred significant additional systematics. It is possible that nonperturbative effects differ between  $W$  and  $Z$  boson production; for instance effects of the charm quark mass may cause a systematic uncertainty in the  $p_T(W)$  prediction and the  $W$  boson mass of a few megaelectronvolts. Initial investigations of such systematics are encouraging (46), however, and they indicate that these effects are unlikely to be an appreciable source of systematic uncertainty.

#### 4.5. External Inputs to Systematics

The key external inputs are the PDFs and the QED radiative corrections. During the Run I analyses rigorous methods of propagating uncertainties in the PDFs were not available. The  $W$  mass uncertainty was evaluated by comparing simulated events that used different parameterizations of PDFs as inputs. The choice of PDFs to compare was heuristic and was based partly on the differences in the data sets used in the global fits. The Run II analyses use improved tools that were not available during Run I; we discuss these tools in Section 5.6.

An important input to the PDF constraints is the Tevatron measurement of the lepton charge asymmetry as a function of rapidity in  $W$  boson decay. The lepton charge asymmetry is a consequence of the  $W$  boson charge asymmetry at production, which is related to the ratio of  $d$  and  $u$  quark distributions in the proton. Continued improvement in the lepton charge asymmetry

measurement, which is statistics limited in the forward-rapidity region, will provide an important constraint on the PDFs (47). A review of the measurement of the lepton charge asymmetry from the Run I data can be found elsewhere (48). Both CDF and DØ have performed measurements of the lepton charge asymmetry with early Run II data (see References 49 and 50; a more recent, preliminary analysis of  $1 \text{ fb}^{-1}$  of integrated luminosity can be found at <http://www-cdf.fnal.gov/physics/ewk/2007/WChargeAsym/PubNote/>), and measurements with greater statistics will be performed.

The uncertainty on QED radiative corrections is dominated by missing higher order corrections. Improved calculations are now available and have been used in the Run II analyses, as we discuss below.

## 5. TEVATRON RUN II $W$ MASS ANALYSES

At the end of Run I, the Tevatron accelerator and the CDF and DØ detectors underwent five years of extensive upgrades. The accelerator complex was upgraded for a factor of 10–20 increase in instantaneous luminosity as well as an increase in the collision center-of-mass energy from 1.8 TeV to 1.96 TeV. The bunch crossing time was reduced from  $\approx 3.5 \mu\text{s}$  in Run I to 396 ns in Run II. The detectors were upgraded for improved performance and for recording data at substantially higher rates.

### 5.1. CDF and DØ Run II Detector Upgrades

The replaced or upgraded components of CDF include the silicon vertex detector, the central drift chamber for tracking, the plug calorimeters for  $|\eta| > 1$ , the muon detector system, and the luminosity monitor (51). The front-end readout electronics, the trigger systems (52), and the data acquisition system, as well as the offline computing systems, were also upgraded. A new time-of-flight detector, a preshower detector, and an EM calorimeter timing system were installed. The CDF upgrades are described in detail in References 20, 53, 54.

From the perspective of the  $W$  boson mass measurement, the important detector upgrades are the central drift chamber (55), the muon detector system, and the plug calorimeters (56). As discussed below, the drift chamber underpins the CDF analysis in Run II. In Run I the Central Tracking Chamber (CTC) generated at most 84 hits on a fiducial track. It was replaced in Run II by the Central Outer Tracker (COT), which generates up to 96 hits, has a drift distance of  $\approx 8 \text{ mm}$  (reduced from  $\approx 5 \text{ cm}$  in the CTC) to reduce the readout time, and has more robust stereo tracking capability.

The CDF plug calorimeter was upgraded from a gas calorimeter to a scintillating-tile calorimeter, with a corresponding reduction in readout time. The calibration of the plug calorimeter is easier to perform with the upgraded detector, allowing more robust measurements of electrons, photons, and hadronic activity in the high-rapidity region. Apart from the upgrade to the CDF muon system readout electronics, the salient muon system upgrades include the installation of new muon detectors for greater azimuthal and rapidity coverage.

The DØ detector underwent even more significant changes and upgrades (57). The central tracking detector is completely new and now includes a silicon microstrip tracker and a scintillating-fiber tracker located within a 2-T solenoidal magnet (58–60). For improved electron identification, new preshower detectors were added between the magnet and the central calorimeter (CC,  $|\eta| < 1$ ) and in front of the end-cap calorimeters (ECs). In the muon systems (61), active detectors were replaced and extended with different technologies for improved triggering. To withstand the harsh radiation environment, additional shielding has been added. The readout

electronics and trigger systems (61, 62) were significantly upgraded in response to the large reduction in bunch spacing time and the higher event rates. The data acquisition systems and the offline systems were replaced.

As discussed in Section 4, the calorimeter was the centerpiece of the DØ Run I measurements of the  $W$  boson mass. The calorimeter itself has not been changed since Run I, so the drift time across the LAr gaps is still 450 ns. The readout electronics, however, were upgraded significantly. New preamplifiers and signal-shaping electronics were installed, and analog pipelining was introduced. The new shapers use only two-thirds of the charge collected by the preamplifier circuit, corresponding to the first  $\simeq 260$  ns of signal from the gaps. The shaper circuit produces a unipolar signal with a peak at about 320 ns and a return to zero after  $\simeq 1.2$   $\mu$ s. The shaped signals are sampled every 132 ns, including samples close to the peak. Upon receiving an accept from the hardware-based stages of the trigger system, the sample at the corresponding peak and the sample taken 396 ns earlier are retrieved from analog memory and the analog difference (known as baseline subtracted signal) is digitized. Subsequently zero-suppression is applied to the data. The suppression thresholds are significantly higher than in Run I; the choice to raise them was driven by the higher noise levels.

Moreover the environment in which the calorimeter operates has changed significantly. The most important of these changes concerns the large amount of uninstrumented material (from the point of view of calorimetric energy measurements) in front of the DØ calorimeter. For example, in the CC the radiation lengths of material between the interaction region and the first active LAr gap is now about  $4.0 X_0$  at normal incidence (increased from  $\approx 1 X_0$  in Run I), which corresponds to  $7.2 X_0$  at the most extreme angles that are encountered for CC electrons.

Another important aspect of Run II that affects CDF and DØ is the large additional transverse energy flow from multiple  $p\bar{p}$  interactions. For example the net measured transverse energy flow from additional  $p\bar{p}$  interactions (from the concurrent and previous crossings) averaged over the so-called Run IIa data-taking period (2001–2006) is already comparable to the flow from the spectator partons in the  $p\bar{p} \rightarrow W + X$  interaction. The relative importance of the additional  $p\bar{p}$  interactions has further increased since then because of the steady increase of instantaneous luminosities delivered by the Tevatron.

## 5.2. Impact of Upgrades on Analysis Methodology

With regard to the CDF analysis methodology, the COT has excellent coverage, efficiency, and resolution. A tracking efficiency for isolated particles in excess of 99% and a single-hit resolution of  $\mathcal{O}(150 \mu\text{m})$  have been achieved. The resolution on inverse momentum (which is proportional to track curvature) is  $\delta p_T^{-1} \approx 0.0015 \text{ GeV}^{-1}$  using only COT hits in the fit; the resolution improves to  $\delta p_T^{-1} \approx 0.0005 \text{ GeV}^{-1}$  for prompt particles when beamline coordinates are included in the fit. The high efficiency and resolution for the lepton tracks from boson decays are major factors in the CDF Run II analysis, as they allow the momentum-scale calibration to rely upon tracking for both the muon and electron decay channels.

Because the leptons from  $W$  and  $Z$  bosons and the  $\Upsilon$  are produced promptly and can be beam constrained, adding the hits from the silicon vertex detector does not significantly improve the track resolution. Therefore the CDF analysis does not use silicon detector hits in the lepton track reconstruction and fitting. One of the benefits of this choice is that any subtle misalignments between the silicon sensors as well as between the silicon detector and the COT do not bias the track measurement.

A side effect of the upgrade to a more powerful silicon detector is that the passive material traversed by the muons and electrons increased substantially from Run I to Run II. This effect has

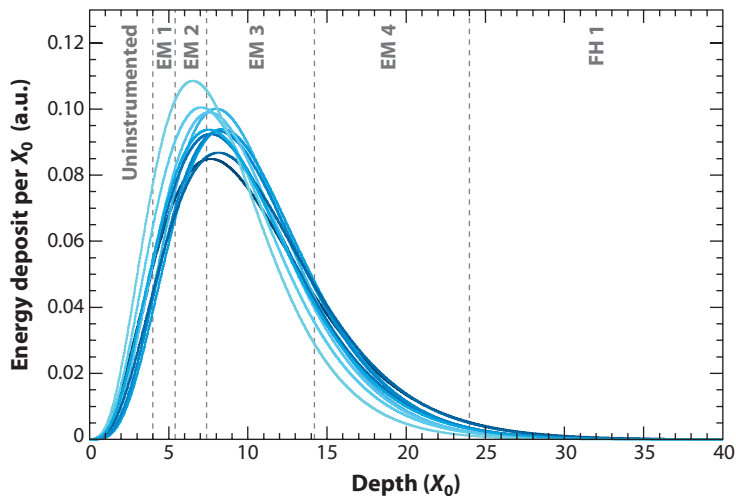
increased the multiple scattering for muons from  $J/\psi$  and  $\Upsilon$  decays and has also increased the rate of electron bremsstrahlung and subsequent photon conversions. A careful accounting of the detector mass and material properties was performed and modeled. The passive material model was cross checked and tuned using collider data on converted photons from  $\pi^0$  decays, the  $p_T$  dependence of the measured  $J/\psi$  mass, and the measured bremsstrahlung spectrum off electrons.

The upgrade of the CDF plug calorimeter enabled researchers to make more reliable measurements of the hadronic recoil in  $W$  and  $Z$  boson events. Because the rapidity distribution of the hadrons is approximately uniform and is uncorrelated with their  $p_T$  distribution, about two-thirds of the recoil transverse energy is detected in the plug calorimeters. CDF used hadron tracks to calibrate the relative response of the central and plug calorimeters, thereby making the calorimeter response more uniform as a function of rapidity. The final calibration of the recoil transverse energy was performed using  $p_T$  balance in  $Z$  boson decays to leptons; the uniformity of the response in rapidity renders the recoil calibration largely insensitive to possible differences in the rapidity distribution of the recoiling particles between  $W$  and  $Z$  boson events.

As discussed above, DØ in Run II has magnetic central tracking, which means that measurement of the  $W$  boson mass in the  $W \rightarrow \mu\nu$  channel is now possible. As the tracking system must fit inside the central calorimeter (reused from Run I; inner diameter 1.42 m), the lever arm in track fitting is short and consequently the curvature resolution is relatively poor:  $\delta p_T^{-1} \simeq 0.0024 \text{ GeV}^{-1}$ . This translates into an experimental  $Z \rightarrow \mu\mu$  mass resolution of 8 GeV, which is significantly worse than the experimental mass resolution in  $Z \rightarrow ee$  (e.g., 2.8 GeV for the subsample where both electrons are in the CC). More importantly, in the muon channel the boson mass resolution is large compared to the natural width of the  $Z$  boson [ $\Gamma_Z = 2.4952 \pm 0.0023 \text{ GeV}$  (21)], i.e., the poor experimental mass resolution significantly reduces the statistical power of each  $Z \rightarrow \mu\mu$  event used in momentum-scale calibrations. The mass resolution is also a limiting factor in detailed studies of momentum-scale uniformity (in terms of different regions of the detector and in terms of  $p_T$ ). The main channel for the  $W$  boson mass measurement at DØ remains the  $W \rightarrow e\nu$  decay with calorimetric electron energy measurement. Confirmation of electron candidates by central tracking provides substantial reduction of fakes from QCD jets, and central tracking provides a precise measurement of the electron direction.

The changes implemented during the upgrade have had a significant impact on the DØ methodology. The change in calorimeter integration time has given rise to new nonuniformities in the calorimeter response that were not present in Run I, and it has significantly amplified some of the small nonuniformities that were already present. The underlying cause of these effects is the nonuniformities in the mechanical structure of the calorimeter modules. Variations in the thickness of the uranium absorber plates from one readout cell to another lead to variations in the response, independent of the integration time. Other types of nonuniformities lead to small response nonuniformities when essentially all charge is read out (as in Run I) but to sizeable nonuniformities when only a fraction of the charge is read out (Run II). A striking example of the latter effect in Run II that leads to  $\mathcal{O}(2\%)$  contribution to the constant term in the calorimeter energy resolution before corrections is the spread in position of the readout boards between two neighboring absorber plates. Another example is the effect of the  $\phi$  cracks between the 32 azimuthal modules of the EM section of the CC. Due to the reduction in integration time, the size of the region close to the module edges that would have to be cut out to eliminate the effect of the cracks has roughly doubled from 20% of the CC acceptance in Run I (12) to 40% today.

The DØ group has developed new methods based on relatively inclusive events collected using dedicated calibration triggers during normal collider data-taking to measure and correct for variations in the energy response from one readout cell to another. Similar techniques are used for both the EM and hadronic (63) sections of the calorimeters. As in Run I (12), the regions near cracks are



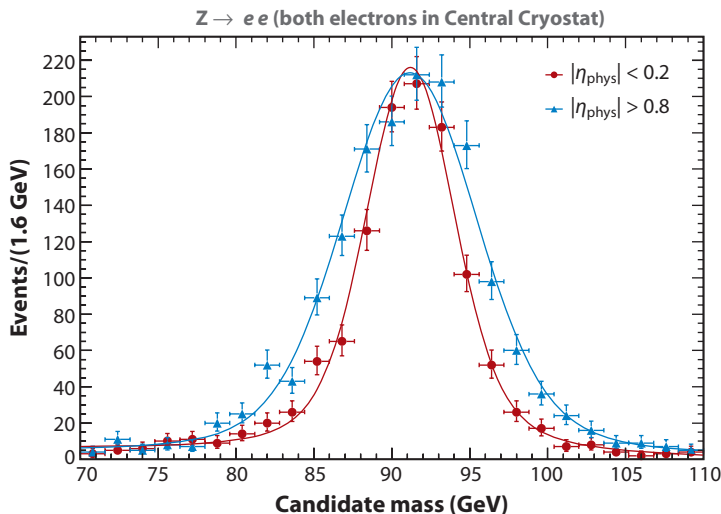
**Figure 5**

Illustration of partial sampling of showers in DØ Run II. The profile of the longitudinal energy depositions from ten electron showers at  $E = 45$  GeV is simulated using the GFLASH (64) parameterized shower model. The ten energy profiles are superimposed in the plot (*solid lines*). The positions of the four electromagnetic (EM) layers (EM1–EM4) and the first hadronic layer (FH1) of the DØ calorimeter, assuming normal incidence, are also indicated (*dashed lines*). The energy deposition is shown in arbitrary units.

studied using subsamples of  $Z \rightarrow ee$  events with electrons detected therein. In Run I the cracks were excluded from the first measurement of the  $W$  boson mass, and a refined measurement including the crack electrons was published later (12). In Run II this separation is no longer practical.

In the DØ Run I analysis, the effect of the uninstrumented material in front of the first active layer of LAr was taken into account using a small energy offset  $\delta_{EM}$  in the electron energy response model (10). The mean reconstructed electron cluster energy  $E(e)$  was described as  $E(e) = \alpha_{EM} E_0 + \delta_{EM}$ , where  $E_0$  denotes the true electron energy. The value of  $\delta_{EM} = -0.16^{+0.03}_{-0.21}$  GeV was measured using  $Z \rightarrow ee$  data and lower energy  $J/\psi \rightarrow ee$  and  $\pi^0 \rightarrow \gamma\gamma$  data. The impact of the uninstrumented material has increased dramatically in Run II because large parts of the typical shower are no longer sampled (shown in **Figure 5**).

The partial sampling has multiple consequences. The calorimeter energy response now has a strong dependence on the angle of impact on the CC, because the amount of material seen by a shower depends on the angle of impact. At a given angle, the response has a nontrivial energy dependence, as the average position of the shower maximum increases logarithmically (65) with energy. At a given angle and energy, the fractional energy deposited in the uninstrumented region varies strongly from one shower to another due to fluctuations in showering. These fluctuations represent a significant contribution to the energy resolution. Furthermore, in the absence of miscalibrations and noise the resolution is no longer described by a single sampling term. As with the response, the resolution is a complicated function of energy and angle of incidence. At normal incidence, and at energies close to 45 GeV, the resolution can be described by a sampling term of  $0.19 \text{ GeV}^{-1/2}$ , which is (as expected) worse than the Run I sampling term of  $0.135 \text{ GeV}^{-1/2}$ . At the same energy and at more extreme angles ( $|\eta| \sim 1$ ), the resolution degrades by another factor of two (illustrated in **Figure 6**). For Run II, DØ developed completely new parameterizations of the calorimeter response and resolution, along with completely new techniques to determine the values of the many new parameters.



**Figure 6**

Reconstructed  $Z \rightarrow ee$  mass distribution in  $1 \text{ fb}^{-1}$  of  $D\bar{O}$  Run II data. The red (blue) distribution corresponds to events where both electrons reach the CC at normal (highly nonnormal) incidence (66).

In Run I,  $D\bar{O}$  measured  $u_T$  with a response of 70% for boson  $p_T > 1.5 \text{ GeV}$  and a resolution sampling term of  $(0.49 \pm 0.14) \text{ GeV}^{-1/2}$  (10). The resolution arises from a combination of many effects, such as neutrinos in the recoil and particles escaping the angular coverage of the calorimeter, which did not change from Run I, as well as the calorimeter response and resolution for charged hadrons, which changed significantly in Run II. The hadronic energy resolution in the  $D\bar{O}$  U/LAr calorimeter depends on the ability to detect clouds of small individual energy deposits from thermalized neutrons (67). In Run II these deposits are read out less efficiently than in Run I because of the shorter integration time (thermalization is slow on the timescale of the Run II integration time) and the tight zero-suppression thresholds. In Run II the sampling term in the recoil resolution is close to  $0.8 \text{ GeV}^{-1/2}$ .

In Run I the simulation of the spectator parton and additional  $p\bar{p}$  interactions was based on data collected using a minimum-bias trigger and an underlying event scale parameter determined from  $Z \rightarrow ee$  data. The particles from these interactions and the particles recoiling against the boson were treated as independent, i.e., the measured transverse energy fluxes from the two contributions were treated as additive. In Run II the two components are correlated in  $D\bar{O}$  because of the tight zero-suppression thresholds: In the presence of a significant energy flow from the additional interactions, the response for the particles balancing the boson  $p_T$  increases because readout cells are more likely to pass the zero-suppression threshold. The corresponding increase in response can be up to 30% at low boson  $p_T$ . Similar effects must be taken into account in the precise determination of the  $D\bar{O}$  jet energy scale (68). In the latter case the corrections are taken from a detailed detector simulation based on GEANT (69). The GEANT-based simulation is not expected to predict the precise values of all parameters in the  $W$  mass parametric detector model. However, it can model the subtle detector effects discussed above at the right order of magnitude, and it can be used to check the validity of the parametric models as well as the methods that are used to extract the parameter values from  $Z$  boson data. In order to validate the  $W$  mass analysis procedure, the  $D\bar{O}$  group uses the same methods as for collider data to perform entire  $W$  boson mass measurement on Monte Carlo  $Z$  and  $W$  boson events from the detailed GEANT-based

simulation. The values of all parameters in the detector model, as well as the measured  $W$  boson mass, are checked against the values obtained using Monte Carlo truth information.

### 5.3. Details of the CDF Run II Analysis

The first CDF Run II analysis, with the result  $M_W = 80,413 \pm 48$  MeV, was recently published (19, 20). The analysis performed a momentum-scale calibration with the COT tracker, which was then transferred to the EM calorimeter using the ratio of calorimeter energy to track momentum  $E/p$  of electrons from  $W$  boson decays. The result was extracted from maximum-likelihood fits to the  $m_T$ ,  $p_T(\ell)$ , and  $p_T(\nu)$  distributions.

The  $W$  and  $Z$  bosons in both the electron and muon channels were triggered inclusively on the presence of a single high- $p_T$  lepton. A hardware-level COT track trigger (52) was used to identify high- $p_T$  tracks. These were matched spatially and temporally (again at the hardware level) to track-segments detected in the muon chambers, or to clusters of high-energy towers in the EM calorimeter. The resolution of the hardware-level quantities such as  $p_T$  and calorimeter transverse energy  $E_T$  was enough to substantially suppress the background rate. If an electron or a muon was detected, the event was read out and another, software-based filter was applied. At this stage full event reconstruction in real time was performed and more stringent criteria were applied for inclusive lepton selection, including the use of reconstructed quantities to provide improved resolution. Events passing the software filter were recorded on magnetic media for later analysis.

In order to minimize the biases in track reconstruction due to misalignments and deformations of the drift chamber, the CDF analysis used a large sample of cosmic rays that diametrically traversed the fiducial volume of the COT. These cosmic ray data were continuously acquired concurrently with collider data using the signal muon trigger. A specialized reconstruction procedure was used to fit the entire trajectory of the cosmic ray muon to a single helix (70). Because this fit incorporated many constraints, aligning the COT cells with respect to these fitted tracks suppressed misalignments that cause curvature and impact parameter biases. Individual cell alignment improved from  $\mathcal{O}(50 \mu\text{m})$  precision with the optical survey to  $\mathcal{O}(5 \mu\text{m})$ . As a cross check, the ratio  $E/p$  was compared between positrons and electrons from  $W$  boson decays. Because the calorimeter responses for high-energy electrons and positrons are essentially identical, a difference in  $E/p$  between them indicated a track curvature bias. Although the bulk of the alignment biases were eliminated by the cosmic ray method, an empirical correction based on the  $E/p$  difference was applied to tracks to remove the residual curvature bias.

As the CDF analysis is anchored on tracking, a first-principles custom tracker simulation was developed for the first Run II analysis. The simulation encoded the equations for multiple scattering and energy loss by ionization and bremsstrahlung and for pair production  $\gamma \rightarrow ee$  and Compton scattering of bremsstrahlung and radiative photons. A three-dimensional geometry describing the material properties as a function of  $(r, \phi, z)$  was used in order to capture the details of EM energy and particle flow in the vicinity of the leptons. About 90% of the passive material traversed by the leptons in the tracking volume is presented by the beam pipe, the silicon vertex detector, and the latter's associated readout infrastructure. The average number of radiation lengths at normal incidence is  $\approx 20\%$ , and the average ionization energy loss per track is  $\approx 9$  MeV. The lepton tracks were propagated in the simulation in small radial steps, generating hits in the COT active volume according to a resolution and efficiency model that was tuned on the collider data. A helical fit was performed to these hits, where the fit included a beam constraint for leptons from  $W$ ,  $Z$ , and  $\Upsilon$  decays. Accompanying photons and conversion electrons were also propagated to the calorimeter, and their energy was combined with the primary lepton energy deposition to simulate the cluster (if they impact the same towers).

The simulation of electron and muon energy deposition in the calorimeter was based on parameterizations and distributions that were either tuned on the collider data or derived from collider data directly. For muons the distribution of the ionization energy loss in the calorimeter was measured from cosmic rays. There is also a contribution of energy flow into the leptons' towers from the underlying event accompanying the hard scatter, as well as from additional proton-antiproton collisions in the same bunch crossing. The distribution of this energy flow was measured in the  $W$  boson data from the energy detected in towers adjacent to the lepton. The electron energy deposition was parameterized with a straight-line response function and a resolution function consisting of a sampling term and a constant term. The sampling term,  $\sigma_E/E = 13.5\%/\sqrt{E_T}$ , was fixed at the value measured in test-beam data, leaving the constant term  $\sigma_E/E = \kappa$  to be constrained from collider data. The first  $D\bar{O}$  measurement from Run II is not yet available, but it is expected to be released in the near future.

#### 5.4. Calibrations in the CDF Analysis

In the CDF analysis (19, 20), the calibration of the tracker momentum scale was performed using mass fits to the  $\mathcal{J}/\psi \rightarrow \mu\mu$  and  $\Upsilon \rightarrow \mu\mu$  decays. The muons from  $\mathcal{J}/\psi$  decays span a range of curvature, allowing the energy-loss model to be pinned down with high precision by studying the variation of the fitted  $\mathcal{J}/\psi$  mass with curvature. A small empirical correction was made to the energy-loss model such that the fitted  $\mathcal{J}/\psi$  mass was independent of muon curvature, within statistical uncertainty. The  $\Upsilon$  mass fit yielded a consistent measurement of the momentum scale, and also provided confirmation that the beam-constraining procedure did not bias the track curvature. In this calibration the dominant systematic uncertainties arose from the imperfect description of these narrow lineshapes by the simulation and from the nonuniformity of the magnetic field, which affects these tracks differently from the  $W$  bosons' decay leptons. These systematics are likely reducible with further study. Using these calibrations, the  $Z$  boson mass fit to the  $Z \rightarrow \mu\mu$  sample yielded the value (see **Figure 7**)  $M_Z = 91,184 \pm 43$  (stat) MeV, which is consistent with the world average (21, 71) and provides a very important cross check of the momentum scale obtained from the  $\mathcal{J}/\psi$  and  $\Upsilon$  mass fits.

The electron channel measurement was made using the calorimeter energy, as the track momentum is significantly affected by external bremsstrahlung. The calorimeter energy response can be calibrated using two techniques: (a) the  $Z \rightarrow ee$  mass measurement and (b) the ratio  $E/p$  of the nonradiative electrons that form a peak near unity. Even though only about half of the electrons from  $W$  boson decay lie in this peak region, this method still provides the best statistical precision because the  $E/p$  peak is quite narrow (see **Figure 8**) and because the  $W$  boson sample is much larger than the  $Z$  boson sample. In addition the  $E/p$  peak fit can be performed in bins of electron  $E_T$  to constrain the nonproportionality of the EM calorimeter response. The peak position is sensitive to the bremsstrahlung spectrum and rate, which were simulated with care (see Reference 20 for details). The rate was constrained by measuring the fraction of radiative electrons (i.e., large  $E/p$ ) and comparing it with the prediction of the simulation. The comparison confirmed that the bremsstrahlung model was accurate within the statistical uncertainty of the data. The energy-scale calibration from the  $Z \rightarrow ee$  mass fit (see **Figure 7**) was found to be consistent with the  $E/p$ -based calibration; the latter yields  $M_Z = 91,190 \pm 67$  (stat) MeV, consistent with the world average (21, 71). This is a very important consistency requirement and provides much confidence in the electron channel measurement. To achieve maximum precision the final result used the combination of both methods, in which the  $E/p$ -based calibration and the  $Z \rightarrow ee$  mass calibration contributed with weights of approximately 2:1.

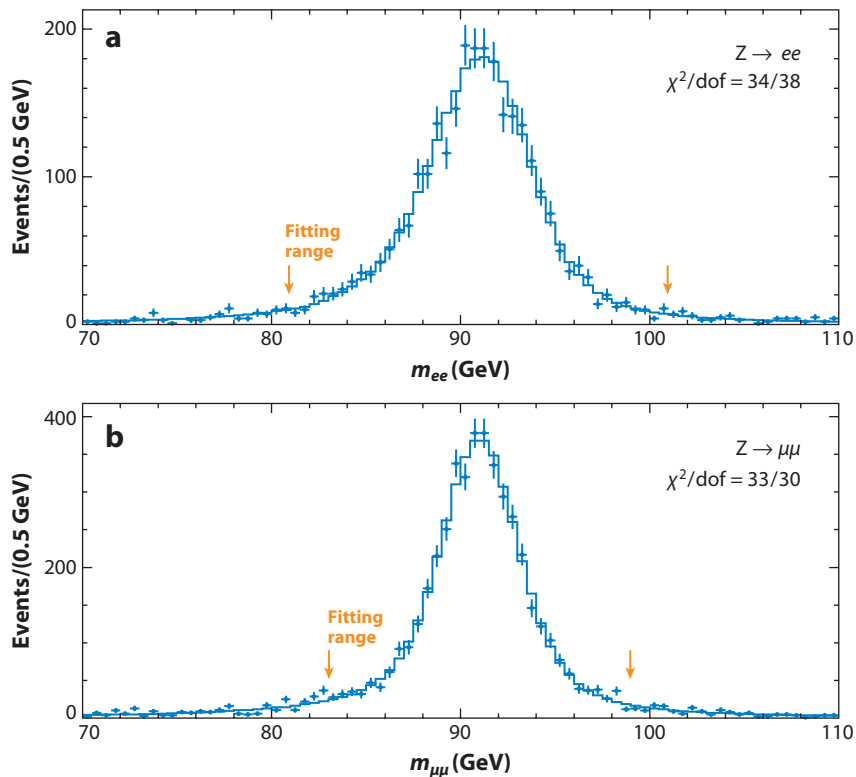


**Figure 7**

The  $Z \rightarrow \mu\mu$  (a) and  $Z \rightarrow ee$  (b) mass fits from the CDF Run II analysis (19, 20), showing the data (points) and the simulation (histogram). The orange arrows indicate the fitting range.

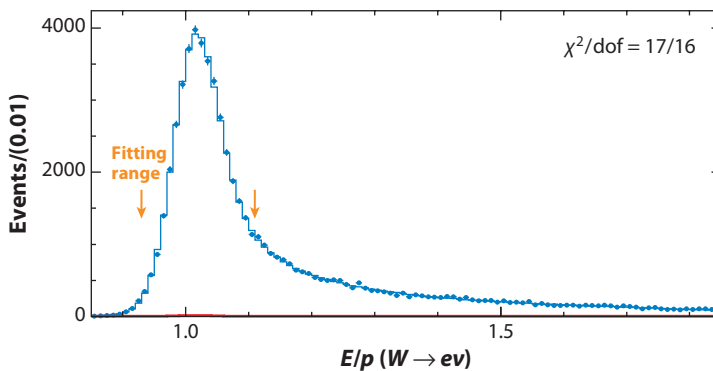


**Figure 8**

The distribution of  $E/p$  for the  $W \rightarrow ev$  data (points) and the best-fit simulation (histogram), including the small jet background (shaded), from the CDF Run II analysis (19, 20). The orange arrows indicate the fitting range used for the electron energy calibration.

The tracking resolution model contained two parameters, the individual hit resolution and the transverse size of the beam spot. The hit resolution was tuned on the observed width of the  $\Upsilon \rightarrow \mu\mu$  mass distribution without applying the beam constraint to the tracks. The width of the  $Z \rightarrow \mu\mu$  mass distribution, where the resolution of the high- $p_T$  muons is more sensitive to the beam constraint, was used to tune the size of the beam spot. With this tracking resolution model, the observed width of the  $E/p$  peak was used to tune the constant term in the calorimeter resolution model. The observed width of the  $Z \rightarrow ee$  mass peak provides an independent measurement of the constant term. The CDF analysis finds that when both electrons are nonradiative (i.e., small  $E/p$ ), the  $Z \rightarrow ee$  mass peak and the  $E/p$  peak provide consistent measurements of the constant term. However, when a significant amount of calorimeter cluster energy is deposited by bremsstrahlung photons and conversion electrons, the corresponding  $Z \rightarrow ee$  subsamples indicate that the cluster energy resolution is degraded. Additional data may be able to shed light on the reason for this effect. In the analysis, an additional resolution contribution was included in the model and applied only to the radiated energy.

### 5.5. Calibrations in the $D\bar{O}$ Analysis

Thus far the  $D\bar{O}$  analysis is based on the  $W \rightarrow e\nu$  channel, and the electron energy is measured using the calorimeter. The calorimeter energy scale is calibrated using mainly  $Z \rightarrow ee$  events, plus  $J/\psi \rightarrow ee$  events to check that the calibration obtained at the  $Z$  mass can be extrapolated to significantly smaller energies. The corrections for the energy lost in the uninstrumented regions (see Section 5.2) are based on a detailed GEANT-based simulation of the  $D\bar{O}$  detector. This simulation includes a precise accounting of the material distribution in the detector, including detailed descriptions of nonuniformities such as the windings of superconductor in the solenoid. The up-to-date cross sections for EM processes are incorporated into GEANT by  $D\bar{O}$ , and the particle tracking inside GEANT is configured to use the highest level of precision. The key experimental inputs for tuning the simulation are the distributions of energy in the longitudinal sections of the EM calorimeter. The sample of  $Z \rightarrow ee$  events is split into subsamples of 15 different angular combinations (using the same approach shown in **Figure 6**), and the distributions of the  $4 \times 15 = 60$  per-layer energy distributions in the four EM layers are checked between data and detailed simulation. Good agreement, within the statistical uncertainties of the collider data, is achieved after tuning five free parameters in the detailed simulation: the absolute energy scale of each of the four readout sections and a small amount of uninstrumented material missing from the material map in the full simulation. The adjusted full simulation is then used to derive energy- and  $\eta$ -dependent parameterizations of energy response and sampling resolution. After this adjustment, the  $Z$  boson mass, measured separately in all of the 15 subsamples, is found to be consistent between subsamples. The constant term in the energy resolution, measured from the width of the 15 mass distributions, is also found to be consistent between subsamples. As in Run I, the absolute energy scale is determined using the precise world average of the  $Z$  boson mass (21), which is utilized as an input to the simulations.

### 5.6. Backgrounds

The background sources can be categorized according to whether the lepton candidates are true prompt leptons from other SM processes, or whether they are hadrons misidentified as leptons due to detector effects. In general sources in the former category can be reliably calculated because the cross sections, decay rates, and angular distributions of the corresponding SM electroweak physics processes are well known, and because the detector acceptances for these final states

are well understood from a full detector simulation. On the other hand, the misidentification backgrounds arise from QCD-hadronic processes, which have much larger cross sections than the electroweak signal but which are suppressed by lepton misidentification rates of  $\mathcal{O}(10^{-3})$ . Thus the hadronic background events form a small but highly sculpted subset of events in the tail of large parent distributions and are very difficult to simulate from first principles. For this latter category of backgrounds, various data-based techniques are devised to extract their rates and kinematic distributions. Because these background distributions are already sculpted by the online trigger requirements, the signal-trigger data sets are used as the base sample for these methods.

The electroweak physics processes generating backgrounds in the  $W$  boson samples are the  $W \rightarrow \tau\nu$  and  $Z \rightarrow \ell\ell$  processes; other electroweak processes have negligible cross sections. The  $\tau$  lepton decays to leptons and hadrons with well-known branching ratios. Both sources of background can be calculated using a full detector simulation and reconstruction, including the  $\tau$  decay to charged and neutral hadrons that can mimic electrons. The  $\tau$  decay polarization is accounted for (72), as it impacts the momentum distribution of the decay products in the laboratory frame. The  $Z \rightarrow \ell\ell$  process can mimic  $W$  boson decays if one of the leptons is undetected or misreconstructed such that its undetected transverse energy mimics a neutrino. For the electron channel, this background is small because the EM calorimeter coverage is fairly complete. For the muon channel, this background is appreciable because a muon outside the acceptance of the central barrel is difficult to track; nevertheless it is well-calculable as it is essentially a geometric effect.

The  $W$  and  $Z$  events selected by the CDF online triggers and offline selection are fairly pure, with misidentification backgrounds constituting about 0.5% of the candidate sample. The analysis requires  $p_T(\ell) > 30$  GeV,  $p_T(\nu) > 30$  GeV, and  $u_T < 15$  GeV, which preserve  $W$  boson events containing the mass information while suppressing the QCD jet background that preferentially populates the low- $p_T(\nu)$ , high- $u_T$  region. Misidentification backgrounds could be suppressed further with tighter cuts on identification quantities, such as isolation energy in the vicinity of the lepton and the number of hits on the track. However, tighter cuts increase the correlation between lepton identification efficiency and the boson  $p_T$ , which biases the lepton  $p_T$  distributions and the mass fits. Hence identification variables that are only weakly influenced by hadronic activity are used for event selection.

## 5.7. Production and Decay Model

For the Run II analyses, CDF and DØ are using the ResBos generator (39), which we discussed in Section 4.2. Although the  $W$  boson decay angular distribution is specified at Born level by its  $V-A$  (left-handed) coupling, it receives  $p_T(W)$ -dependent corrections due to kinematic boosting and QCD dynamics. These corrections have been calculated and compared to the data (73, 74). The ResBos (39) and DYRAD (75) programs incorporate these  $p_T(W)$ -dependent corrections to the decay angular distribution. As the precision of the  $W$  boson mass measurement continues to improve at hadron colliders, higher order calculations will likely be needed.

The full quintuple differential cross section for  $W$  and  $Z$  boson production and decay from ResBos provides a unified model for describing these events. A particle-level description of the hadronic recoil is not needed as the recoil is reconstructed inclusively using calorimetric energy flow. To the extent that the model simultaneously describes  $Z$  and  $W$  boson production, the  $Z$  boson events can be used to tune the parameters of the model. For example, in the CDF Run II analysis the dilepton  $p_T$  spectrum in the  $Z$  boson events is used to constrain the dominant parameter in the nonperturbative form factor, which is then used as an input for predicting the  $p_T(W)$  spectrum. The constraints from the  $Z$  boson data have become sufficiently precise that possible differences between  $Z$  and  $W$  boson dynamics may need to be corrected for (46).

QED radiative corrections have been implemented in the CDF Run II analysis using the two-dimensional probability distribution of the radiated photon's energy and angle with respect to the charged lepton. The distribution is calculated using the WGRAD program (45), which is a complete electroweak calculation of radiative corrections at  $\mathcal{O}(\alpha)$ . Higher order photon radiation has been emulated by increasing the leading-order photon energy by an estimated 10% (76), but with a 5% uncertainty assigned. The higher order corrections need to be studied in more detail in order to reduce this source of uncertainty, which will become important when more data are analyzed.

The technique for estimating PDF uncertainties has improved significantly since the Run I analyses were published. The Coordinated Theoretical-Experimental Project on QCD (CTEQ) (77) and the Martin-Roberts-Stirling-Thorne (MRST) (78) sets of PDFs now provide associated ensembles of PDFs, which describe the independent variations of the PDF fit parameters that are permitted by the uncertainties in the global data sets. The corresponding uncertainty on  $M_W$  is obtained by performing a Monte Carlo pseudoexperiment for each PDF in the ensemble by fitting the simulated events using the templates generated with the default PDF and noting the resulting shift in  $M_W$  with respect to its default value. The  $M_W$  shifts due to all the PDF eigenvector pairs are summed in quadrature. This scheme provides a robust procedure for propagating uncertainties in PDFs to any observable. Nevertheless, some ambiguities in the procedure remain. First, if a PDF eigenvector variation is found to map nonlinearly to  $M_W$  (i.e., if the positive and negative variation in the PDF eigenvector does not result in equal, opposite shifts in  $M_W$ ), its contribution to the  $M_W$  uncertainty is not uniquely defined. It would be useful to understand the source of these nongaussian  $M_W$  uncertainties predicted by the PDF variation sets. Second, the confidence interval represented by the PDF ensemble is not calculated analytically from the quality of the global fit. The confidence interval of the CTEQ6 ensemble is estimated to be 90%, and it is used as such in the CDF Run II analysis. As the detector-related uncertainties on  $M_W$  shrink with the analysis of more data, these issues in PDF uncertainty estimation will become more important.

## 6. WHAT HAVE WE LEARNED ABOUT THE HIGGS AND OTHER NEW PHYSICS?

From 200 pb<sup>-1</sup> of data, the CDF Run II analysis measures

$$M_W = 80,413 \pm 34(\text{stat}) \pm 34(\text{syst}) \text{ MeV}$$

by combining the results of the electron and muon transverse mass, lepton, and neutrino  $p_T$  fits using the BLUE (41) method. The  $m_T$  fits contribute 80% of the weight to this combination. Two of the fits are shown in **Figure 4** and the  $m_T$  systematic uncertainties are shown in **Table 4**, along with the systematic uncertainties on the combined result.

**Table 5** summarizes recent measurements and their averages, showing both the impact of the CDF Run II measurement (19, 20) on the Tevatron and the world averages. The Tevatron combination has been updated using the BLUE method (as discussed in Reference 13), with the uncertainties due to PDFs and QED radiative corrections assumed to be fully correlated. The combination of the LEP and Tevatron measurements assumes no correlation. Possible correlation of the QED radiative corrections between the LEP and Tevatron measurements should be explored.

**Figure 9** compares the latest world-average masses of the  $W$  boson (19, 20) and the top quark (18) with the predictions (16, 79) of the SM and the minimal supersymmetric extension of the standard model (MSSM). The measurements are consistent with the SM, although the central

**Table 4** Systematic and total uncertainties in MeV for the  $m_T$  and combined fits in the CDF Run II analysis

Systematic	$W \rightarrow e\nu$	$W \rightarrow \mu\nu$	Common <sup>a</sup>	Combined <sup>b</sup>
$p_T(W)$ model	3	3	3	3.9
QED radiation	11	12	11	11.6
Parton distributions	11	11	11	12.6
Lepton energy scale	30	17	17	23.1
Lepton energy resolution	9	3	0	4.4
Recoil energy scale	9	9	9	8.3
Recoil energy resolution	7	7	7	9.6
Selection bias	3	1	0	1.7
Lepton tower removal	8	5	5	6.3
Backgrounds	8	9	0	6.4
Total systematic	39	27	26	34
Total uncertainty	62	60	26	48

<sup>a</sup>“Common” column shows the correlated uncertainties between the electron and muon channel  $m_T$  fits.

<sup>b</sup>“Combined” column shows the systematic uncertainty on the combined result from both channels, including the  $m_T$ ,  $p_T(\ell)$  and  $p_T(\nu)$  fits. Data is from Reference 20. Abbreviation: QED, quantum electrodynamics.

values show some preference (albeit not definitive) for the MSSM over the SM (16, 79). Performing an electroweak fit within the context of the SM using these latest values of  $M_W$  and  $M_{\text{top}}$  and the methods and data described in References 14 and 80 yields the inferred value of the SM Higgs mass,  $M_H = 76^{+33}_{-24}$  GeV (20). The effect of the CDF Run II measurement of  $M_W$  is to reduce the inferred value of  $M_H$  by 6 GeV (20). The corresponding upper limit is  $M_H < 144$  GeV at the 95% confidence level. It is interesting to compare this confidence interval, derived from precision data alone, with the result of the direct Higgs boson searches at LEP,  $M_H > 114.4$  GeV (81). The combination of these two pieces of information restricts the SM Higgs boson mass to a relatively narrow, low-mass range, with interesting and significant implications for direct searches at the Tevatron and the LHC.

**Table 5** Current world’s best  $W$  boson mass measurements and averages

Experiment	Mass (MeV)
DELPHI	$80336 \pm 67$
L3	$80270 \pm 55$
OPAL	$80416 \pm 53$
ALEPH	$80440 \pm 51$
CDF-I	$80433 \pm 79$
DØ-I	$80483 \pm 84$
LEP average	$80376 \pm 33$
Tevatron-I average	$80454 \pm 59$
World average	$80392 \pm 29$
CDF-II	$80413 \pm 48$
New CDF average	$80418 \pm 42$
New Tevatron average	$80429 \pm 39$
New world average	$80398 \pm 25$

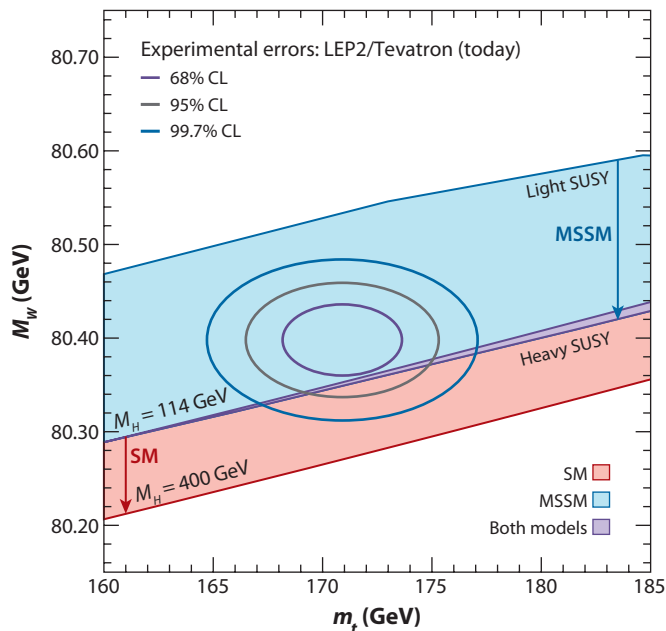


**Figure 9**

The  $1\sigma$ -,  $2\sigma$ -, and  $3\sigma$ -confidence level contours for the world-average  $W$  boson mass (19, 20) and the top quark mass (18), compared with the predictions (16, 79) of the standard model (SM) and the minimal supersymmetric extension of the standard model (MSSM). Figure from Reference 79.

## 7. ULTIMATE $M_W$ PRECISION FROM THE TEVATRON RUN II

The  $M_W$  measurement depends critically on calibration of the lepton momentum, as well as a sufficiently precise and robust understanding of the hadronic recoil and the backgrounds. In addition, because the kinematic quantities to be fit are necessarily transverse kinematics rather than Lorentz-invariant kinematics the theoretical model of  $W$  boson production and decay must have a commensurate level of precision.

As discussed in this and previous reviews and the respective experiments' publications, sophisticated techniques have been developed to constrain the detector and theory models using the collider data. The measurements of  $M_W$  have been performed for the last two decades with samples of increasing statistics, and the total uncertainty has shrunk by a factor of ten, generally scaling with statistics. Over this time period, not only have the analysis techniques improved, but the calculations of  $W$  boson production and decay have been performed to higher order in QCD and QED and the global data constraints on PDFs and boson  $p_T$  have improved considerably. There is every reason to expect that improvements will continue to occur on all these fronts.

CDF and DØ will analyze larger Run II data sets with the goal of statistics scaling of as many of the systematic uncertainties as possible. There will be challenges along the way; for example if the lepton momentum resolution or the recoil resolution degrades due to multiple interactions, the precision will be worse with respect to scaling. Although some loss of resolution is inevitable, in our opinion this will not be a severe effect in itself. A greater challenge is the increase in the number of degrees of freedom needed to adequately describe the response and resolution functions of the leptons and the recoil. We have noted above that the DØ analysis is facing this issue in Run II with respect to Run I. There will likely be tension between the increasing complexity of the models

and the additional data sets that can be used to constrain the new parameters. For instance, if the  $Z$  boson data alone were used to constrain an increasing number of parameters, the measurement precision would degrade with respect to scaling. However, the use of minimum-bias data, jet data,  $\mathcal{J}/\psi$ , and  $\Upsilon$  data to augment the analysis and constrain new parameters has been demonstrated by the CDF Run II analysis. By continuing to add such constraints, scaling can be maintained and even improved upon.

The CDF Run II analysis provides insightful comparisons with the Run I analysis regarding the scaling of uncertainties. The Run II tracking resolution obtained with the COT is better than in CDF Run I, mostly due to the detector upgrade but also due to algorithm and alignment improvements. The electron energy resolution from calorimetry was maintained from Run I to Run II. In the early Run II data used for the publication (19, 20), the rate of multiple interactions was low and did not degrade the recoil resolution. As a result the fit statistical errors have continued to scale with event statistics. For the most important systematic uncertainty, which results from the lepton momentum calibration, the  $\mathcal{J}/\psi$ ,  $\Upsilon$ ,  $W \rightarrow e\nu$ , and  $Z$  boson data have all been used in Run II; this represents an improvement in statistical scaling compared to Run I, where the momentum scale was set using primarily the  $Z$  boson data. Similarly, isolated tracks from minimum bias data were used in Run II to improve the uniformity of the hadronic calorimeter response with respect to rapidity, thereby reducing the reliance on  $Z$  boson data for recoil calibration and improving the  $u_T$ ,  $m_T$  and  $p_T(\nu)$  resolution. Finally, the number of ad hoc parameters in the recoil response and resolution parameterizations, as well as the  $p_T(W)$  parameterization, was smaller in the CDF Run II analysis compared to Run I, but these parameters still provided a consistent description of the data. This reduction in the number of parameters was a result of using physically motivated parameterizations, and it contributed to smaller systematic uncertainties in the Run II analysis relative to scaling. If these models continue to prove adequate with higher statistics, future scaling of these uncertainties can be expected.

The detailed GEANT-based simulation of the detector is also being increasingly exploited to motivate response and resolution parameterizations. Careful first-principles calculations can eliminate ad hoc parameters in some cases and can improve the statistical power of the control data sets. Both CDF and  $D\emptyset$  are utilizing these first-principles calculations more heavily in Run II than in Run I, a trend that is likely to continue.

As we anticipate improvements in PDFs due to new  $W$  asymmetry measurements (49, 50), higher order QED radiative corrections (76), and  $p_T(W)$  parameterizations (46), we can expect Tevatron measurements to improve substantially. While the data in the CDF Run II publication were based on  $200 \text{ pb}^{-1}$ , both CDF and  $D\emptyset$  now analyze  $1\text{--}2 \text{ fb}^{-1}$  and may ultimately analyze about  $6 \text{ fb}^{-1}$ . There is much to learn from the next round of publications from CDF and  $D\emptyset$ ; the CDF group has mentioned its goal of surpassing  $25 \text{ MeV}$  total uncertainty with its  $2\text{-fb}^{-1}$  analysis (82). An ultimate  $M_W$  precision of  $15 \text{ MeV}$  from the Tevatron may be possible.

## 8. SUMMARY

The direct measurement of the  $W$  boson mass is one of the most important precision measurements at high  $Q^2$ —the others are  $M_Z$ ,  $\sin^2\theta_W$ , and  $M_{\text{top}}$ —that constrain the mechanism of electroweak symmetry breaking. The LEP experiments have measured  $M_W$  with a combined precision of  $33 \text{ MeV}$ . Run I at the Tevatron ended with CDF and  $D\emptyset$  publishing a combined hadron collider average with a precision of  $59 \text{ MeV}$ , based on  $100 \text{ pb}^{-1}$  each. Run II at the Tevatron is running successfully, and CDF has recently published its first Run II measurement with a precision of  $48 \text{ MeV}$ , using  $200 \text{ pb}^{-1}$ . The consistent measurements made by CDF and  $D\emptyset$  have yielded a world average  $M_W = 80,398 \pm 25 \text{ MeV}$ . For precision better than  $15 \text{ MeV}$ ,  $M_W$  carries more

weight in the SM fit for  $M_H$  than the weight of  $\sin^2\theta_W$ , given an  $M_{\text{top}}$  uncertainty of 1.5 GeV (M. Chanowitz, private communication). We are entering a new era of stringent electroweak tests of the SM Higgs mechanism in which  $M_W$  will play an increasingly important (even dominant) role and in which measurements of  $M_W$  (and  $M_{\text{top}}$ ) will continue to improve at the Tevatron with the analysis of  $>1\text{-fb}^{-1}$  data sets. It will be interesting to see whether the precision electroweak fits will continue to support the SM, whether they will prefer an alternate theory such as its supersymmetric extension, and how the big picture will evolve with the discovery of new particles.

## DISCLOSURE STATEMENT

The authors are not aware of any biases that might be perceived as affecting the objectivity of this review.

## ACKNOWLEDGEMENTS

We would like to thank our colleagues with whom we have collaborated while working on the  $M_W$  measurement. We appreciate the useful comments on the manuscript from Douglas Glenzinski, Paul Grannis, Christopher Hays, Ronald Madaras, Larry Nodulman, Peter Renton, Oliver Stelzer-Chilton, and David Waters. The work of A.V.K. is partially supported by the U.S. Department of Energy under a grant to Duke University and by the Alfred P. Sloan Foundation.

## LITERATURE CITED

1. Glenzinski DA, Heintz U. *Annu. Rev. Nucl. Part. Sci.* 50:207 (2000)
2. Glashow SL. *Nucl. Phys.* 22:579 (1961); Weinberg S. *Phys. Rev. Lett.* 19:1264 (1967); Salam A. In *Elementary Particle Theory*, p. 367, ed. N Svartholm. Stockholm: Almquist & Wiksell (1968)
3. Arnison G, et al. (UA1 Collab.) *Phys. Lett.* 122B:103 (1983)
4. Banner M, et al. (UA2 Collab.) *Phys. Lett.* 122B:476 (1983)
5. Arnison G, et al. (UA1 Collab.) *Phys. Lett.* 126B:398 (1983)
6. Bagnaia P, et al. (UA2 Collab.) *Phys. Lett.* 129B:130 (1983)
7. Albajar C, et al. (UA1 Collab.) *Z. Phys. C* 44:15 (1989)
8. Alitti J, et al. (UA2 Collab.) *Phys. Lett. B* 241:150 (1990)
9. Affolder T, et al. (CDF Collab.) *Phys. Rev. D* 64:052001 (2001)
10. Abazov VM, et al. (DØ Collab.) *Phys. Rev. D* 58:092003 (1998); Abbott B, et al. (DØ Collab.) *Phys. Rev. D* 58:012002 (1998)
11. Abbott B, et al. (DØ Collab.) *Phys. Rev. D* 62:092006 (2000)
12. Abazov VM, et al. (DØ Collab.) *Phys. Rev. D* 66:012001 (2002)
13. Abazov VM, et al. (CDF and DØ Collab.) *Phys. Rev. D* 70:092008 (2004)
14. Alcaraz J, et al. (ALEPH, DELPHI, L3, OPAL Collab., LEP Electroweak Working Group) arXiv:hep-ex/0612034 (2006)
15. Sirlin A. *Phys. Rev. D* 22:971 (1980)
16. Heinemeyer S, et al. *JHEP* 0608:052 (2006)
17. Awramik M, et al. *Phys. Rev. D* 69:053006 (2004)
18. Brubaker E, et al. (CDF and DØ Collab., Tevatron Electroweak Working Group) arXiv:hep-ex/0703034 (2007)
19. Aaltonen T, et al. (CDF Collab.) *Phys. Rev. Lett.* 99:151801 (2007)
20. Aaltonen T, et al. (CDF Collab.) arXiv:hep-ex/0708.3642 (2007)
21. Schael S, et al, (ALEPH Collab., DELPHI Collab., L3 Collab., OPAL Collab., SLD Collab., LEP Electroweak Working Group, SLD Electroweak and Heavy Flavor Groups) *Phys. Rep.* 427:257 (2006)
22. Barate R, et al. (ALEPH Collab.) *Phys. Lett. B* 401:347 (1997)

23. Abreu P, et al. (DELPHI Collab.) *Phys. Lett. B* 397:158 (1997)
24. Acciarri M, et al. (L3 Collab.) *Phys. Lett. B* 398:223 (1997)
25. Ackerstaff K, et al. (OPAL Collab.) *Phys. Lett. B* 389:416 (1996)
26. Schael S, et al. (ALEPH Collab.) *Eur. Phys. J. C* 47:309 (2006)
27. Abdallah J, et al, arXiv:0803.2534 (2008)
28. Acciarri M, et al. (L3 Collab.) *Eur. Phys. J. C* 45:569 (2006)
29. Abbiendi G, et al. (OPAL Collab.) *Eur. Phys. J. C* 45:307 (2006)
30. Alitti J, et al. (UA2 Collab.) *Phys. Lett. B* 276:365 (1992)
31. Abbott B, et al. (DØ Collab.) *Phys. Rev. D* 60:052003 (1999)
32. Acosta D, et al. (CDF Collab.) *Phys. Rev. Lett.* 94:091803 (2005)
33. Haywood S, et al. arXiv:hep-ph/0003275 (2000)
34. ATLAS Collab. *ATLAS TDR 15, CERN/LHCC 99/15.* (1999)
35. Buge V, et al. *J. Phys. G* 34:193 (2007)
36. Gordon AS. Ph.D. thesis, Harvard Univ. (1998); Adam IM. Ph.D. thesis, Columbia Univ. (1997); Flattum E. Ph.D. thesis, Michigan State Univ. (1996)
37. Abe F, et al. (CDF Collab.) *Nucl. Instrum. Methods A* 271:387 (1988)
38. Abachi S, et al. (DØ Collab.) *Nucl. Instrum. Methods A* 338:185 (1994)
39. Landry F, Brock R, Nadolsky PM, Yuan C-P. *Phys. Rev. D* 67:073016 (2003); Landry F, Brock R, Ladinsky G, Yuan C-P. *Phys. Rev. D* 63:013004 (2000); Balazs C, Yuan C-P. *Phys. Rev. D* 56:5558 (1997); Ladinsky GA, Yuan C-P. *Phys. Rev. D* 50:4239 (1994)
40. Ellis RK, Veseli S. *Nucl. Phys. B* 511:649 (1998)
41. Lyons L, Gibaut D, Clifford P. *Nucl. Instrum. Methods Phys. Res. A* 270:110 (1988)
42. Berends FA, Kleiss R, Revol JP, Vialle JP. *Z. Phys. C* 27:155 (1985); Berends F, Kleiss R. *Z. Phys. C* 27:365 (1985)
43. Wagner RG. *Comput. Phys. Commun.* 70:15 (1992)
44. Barberio E, Was Z. *Comput. Phys. Commun.* 79:291 (1994); Barberio E, van Eijk B, Was Z. *Comput. Phys. Commun.* 66:115 (1991)
45. Baur U, Keller S, Wackerroth D. *Phys. Rev. D* 59:013002 (1999)
46. Berge S, Nadolsky PM, Olness FI. *Phys. Rev. D* 73:013002 (2006); Konychev AV, Nadolsky PM. *Phys. Lett. B* 633:710 (2006)
47. Bodek A, et al. arXiv:0711.2859 (2007)
48. Thurman-Keup RM, Kotwal AV, Tecchio M, Byon-Wagner A. *Rev. Mod. Phys.* 73:267 (2001)
49. Acosta D, et al. (CDF Collab.) *Phys. Rev. D* 71:051104 (2005)
50. DØ Collaboration, Abazov VM, et al. arXiv:0709.4254 *Phys. Rev. D* 77:011106 (2008)
51. Elias J, et al. *Nucl. Instrum. Methods Phys. Res. A* 441:366 (2000)
52. Thomson EJ, et al. *IEEE Trans. Nucl. Sci.* 49:1063 (2002)
53. Acosta D, et al. (CDF Collab.) *Phys. Rev. D* 71:032001 (2005)
54. Abulencia A, et al. (CDF Collab.) *J. Phys. G* 34:2457 (2007)
55. Affolder T, et al. *Nucl. Instrum. Methods Phys. Res. A* 526:249 (2004)
56. Albrow M, et al. *Nucl. Instrum. Methods Phys. Res. A* 480:524 (2002); Apollinari G, et al. *Nucl. Instrum. Meth. Phys. Res. A* 412:515 (1998)
57. Abazov VM, et al. (DØ Collab.) *Nucl. Instrum. Methods A* 565:463 (2006)
58. Lincoln D. (DØ Collab.) *Nucl. Instrum. Methods A* 379:424 (1996)
59. Fast J. (DØ Collab.) *Nucl. Phys. Proc. Suppl.* 125:352 (2003)
60. Lipton R. (DØ Collab.) *Nucl. Instrum. Methods A* 566:104 (2006)
61. Abazov VM, et al. *Nucl. Instrum. Methods A* 552:372 (2005)
62. Abolins M, et al. *Nucl. Instrum. Methods A* 584:75 (2007)
63. Peters K. *AIP Conf. Proc.* 867:17 (2006)
64. Grindhammer G, Rudowicz M, Peters S. *Nucl. Instrum. Methods A* 290:469 (1990)
65. Yao W-M, et al. *J. Phys. G* 33:258 (2006)
66. Buchanan NJ. *AIP Conf. Proc.* 867:3 (2006)
67. Wigmans R. *Calorimetry.* Oxford: Clarendon, 754 pp. (2000) and references therein

68. Abazov VM, et al. (DØ Collab.) [http://www-d0.fnal.gov/phys\\_id/jes/public/plots.v7.1/](http://www-d0.fnal.gov/phys_id/jes/public/plots.v7.1/) (2008)
69. Brun R, Carminati F. *CERN Program Libr. Long Writeup W5013* (unpublished) (1993)
70. Kotwal AV, Gerberich HK, Hays C. *Nucl. Instrum. Methods Phys. Res. A* 506:110 (2003)
71. Yao W-M, et al. *J. Phys. G* 33:1 (2006)
72. Jadach S, Kuhn JH, Was Z. *Comput. Phys. Comm.* 64:275 (1990); Jezabek M, et al. *Comput. Phys. Comm.* 70:69 (1992); Jadach S, Was Z, Decker R, Kuhn JH. *Comput. Phys. Comm.* 76:361 (1993); Was Z, Golonka P. *Nucl. Phys. Proc. Suppl.* 144:88 (2005); Was Z, et al. *Nucl. Phys. Proc. Suppl.* 98:96 (2001)
73. Acosta DE, et al. (CDF Collab.) *Phys. Rev. D* 70:032004 (2004); Acosta DE, et al. (CDF Collab.) *Phys. Rev. D* 73:052002 (2006)
74. Abbott B, et al. (DØ Collab.) *Phys. Rev. D* 63:072001 (2001)
75. Giele WT, Glover EWN, Kosower DA. *Nucl. Phys. B* 403:633 (1993)
76. Carloni Calame CM, Montagna G, Nicosini O, Treccani M. *Phys. Rev. D* 69:037301 (2004)
77. Pumplin J, et al. *J. High Energy Phys.* 0207:012 (2002)
78. Martin AD, Roberts RG, Stirling WJ, Thorne RS. *Eur. Phys. Jour. C* 28:455 (2003); Martin AD, Roberts RG, Stirling WJ, Thorne RS. *Eur. Phys. J. C* 35:325 (2004)
79. Heinemeyer S, et al. *Pramana* 69:783 (2007)
80. Renton PB. *Rep. Prog. Phys.* 65:1271 (2002)
81. Barate R, et al. (LEP Working Group for Higgs Boson Searches, ALEPH Collab., DELPHI Collab., L3 Collab., OPAL Collab.) *Phys. Lett. B* 565:61 (2003)
82. Stelzer-Chilton O. (CDF Collab.) arXiv:0706.0284 (2007); Hays C. (CDF Collab.) *Frascati Physics Series*, p. 231, ed. M Greco, vol. XLIV (2007)



# Contents

Effective Field Theory and Finite-Density Systems <i>Richard J. Furnstahl, Gautam Rupak, and Thomas Schäfer</i> .....	1
Nuclear Many-Body Scattering Calculations with the Coulomb Interaction <i>A. Deluva, A.C. Fonseca, and P.U. Sauer</i> .....	27
The Exotic XYZ Charmonium-Like Mesons <i>Stephen Godfrey and Stephen L. Olsen</i> .....	51
Nonstandard Higgs Boson Decays <i>Spencer Chang, Radovan Dermisek, John F. Gunion, and Neal Weiner</i> .....	75
Weak Gravitational Lensing and Its Cosmological Applications <i>Henk Hoekstra and Bhuvnesh Jain</i> .....	99
Top Quark Properties and Interactions <i>Regina Demina and Evelyn J. Thomson</i> .....	125
Measurement of the $W$ Boson Mass at the Tevatron <i>Ashtosh V. Kotwal and Jan Stark</i> .....	147
Coalescence Models for Hadron Formation from Quark-Gluon Plasma <i>Rainer Fries, Vincenzo Greco, and Paul Sorensen</i> .....	177
Experimental Tests of General Relativity <i>Slava G. Turyshev</i> .....	207
Charm Meson Decays <i>Marina Artuso, Brian Meadows, and Alexey A. Petrov</i> .....	249
Strategies for Determining the Nature of Dark Matter <i>Dan Hooper and Edward A. Baltz</i> .....	293
Charged Lepton Flavor Violation Experiments <i>William J. Marciano, Toshinori Mori, and J. Michael Roney</i> .....	315
Neutrino Masses and Mixings: Status and Prospects <i>Leslie Camilleri, Eligio Lisi, and John F. Wilkerson</i> .....	343